



HAL
open science

High hydrogen release by cryo-adsorption and compression on porous materials

Pamela Ramirez-Vidal, Giuseppe Sdanghi, Alain Celzard, Vanessa Fierro

► **To cite this version:**

Pamela Ramirez-Vidal, Giuseppe Sdanghi, Alain Celzard, Vanessa Fierro. High hydrogen release by cryo-adsorption and compression on porous materials. *International Journal of Hydrogen Energy*, 2022, 47 (14), pp.8892-8915. 10.1016/j.ijhydene.2021.12.235 . hal-03842532

HAL Id: hal-03842532

<https://hal.univ-lorraine.fr/hal-03842532>

Submitted on 7 Nov 2022

HAL is a multi-disciplinary open access archive for the deposit and dissemination of scientific research documents, whether they are published or not. The documents may come from teaching and research institutions in France or abroad, or from public or private research centers.

L'archive ouverte pluridisciplinaire **HAL**, est destinée au dépôt et à la diffusion de documents scientifiques de niveau recherche, publiés ou non, émanant des établissements d'enseignement et de recherche français ou étrangers, des laboratoires publics ou privés.



Distributed under a Creative Commons Attribution - NonCommercial - NoDerivatives 4.0 International License

High hydrogen release by cryo-adsorption and compression on porous materials

Pamela Ramirez-Vidal¹, Giuseppe Sdanghi^{1,2}, Alain Celzard¹, Vanessa

Fierro^{1*}

¹ Université de Lorraine, CNRS, IJL, F-88000 Epinal, France

² Université de Lorraine, CNRS, LEMTA, F-54000 Nancy, France

* Corresponding author. Tel: + 33 372 74 96 77.

Fax: + 33 372 74 96 38.

E-mail address: Vanessa.Fierro@univ-lorraine.fr (V. Fierro)

Abstract

Although hydrogen is a promising energy carrier to replace fossil fuels and reduce CO₂ emissions, its low volumetric energy density remains a major drawback. Indeed, hydrogen storage is one of the main technical obstacles limiting the large-scale use of hydrogen in fuel cell vehicles (FCVs). To solve this problem, there are different technical approaches such as: (i) compression in gas cylinders, (ii) liquefaction in cryogenic tanks, (iii) cryo-compression; and (iii) absorption or adsorption into solids. Cryogenic adsorption pressure systems are a promising approach to hydrogen storage because they require less resistant materials than those needed for compression at 70 MPa at room temperature, and can avoid the gas loss associated with boiling in liquid hydrogen storage systems. In this manuscript, we have reviewed different solutions for hydrogen storage, with a particular focus on hydrogen adsorption at cryogenic temperatures and moderate pressures on high surface area porous materials, namely: activated carbons, hyper-crosslinked polymers and metal organic frameworks. In addition, we discuss the elements involved in the design of rapidly rechargeable, compact, lightweight and cost-effective hydrogen storage systems. We also provide not only hydrogen storage capacities but hydrogen release capacities considering hydrogen at 10 MPa a discharge at 0.5 MPa.

Keywords: hydrogen storage; physisorption; cryo-compression; hydrogen liquefaction; green hydrogen; release capacity

1. Introduction

With the highest gravimetric energy density of all non-nuclear fuels (120 MJ kg^{-1}), (**Figure 1a**) hydrogen is considered as a real alternative to fossil fuels [1]. This is evidenced by the fact that the gravimetric energy density of gasoline (44 MJ kg^{-1}) is one-third that of hydrogen (**Figure 1a**). However, being the lightest element in the universe, it has also the lowest energy density by volume (0.0108 MJ L^{-1} at 298 K, 0.1 MPa) [2]. Therefore, the implementation of an efficient and practical hydrogen storage system is a major challenge.

Although hydrogen is the most abundant element on Earth, less than 1% is present as molecular hydrogen gas. Large streams of natural hydrogen can be produced by geological structures and underwater exudations. However, most hydrogen is primarily chemically bound to other elements, as in the case of water and hydrocarbons, and so energy must be expended to produce it. The energy required to carry out this process can be obtained from fossil or renewable sources [3]. **Figure 1b** summarizes the different synthesis methods currently used for hydrogen production [4]. At present, about 120 Mt of hydrogen is produced each year, of which one-third is a mixture with other gases and the rest is pure hydrogen [5]. About 96% of the hydrogen produced today comes from fossil fuels [6], and natural gas is currently the main source of hydrogen production through steam methane reforming (SMR). [5–7]. Alternative synthesis methods to produce hydrogen are based on anaerobic fermentation of biomass [8,9] and water electrolysis. The main advantage of these solutions is that they allow the use of renewable energy sources, such as solar, geothermal, biomass, ocean heat, and nuclear energy [10–13].

In order to facilitate the identification of the synthesis method used to produce hydrogen, as well as the resulting CO_2 emission, several colors can be associated with hydrogen. The most common known colors of hydrogen are gray, blue, turquoise, yellow and green (**Figure 1b**) [14]. Gray hydrogen is

produced from fossil fuel sources, while blue hydrogen can be produced like gray hydrogen, but with the sequestration or reuse of by-product CO₂. Hydrogen is said to be "turquoise" when it is produced by the thermal fractionation of methane, *i.e.*, by the pyrolysis of methane. In this case, the by-product is solid carbon instead of CO₂, which is a potential feedstock for several industrial applications [15,16]. Compared to gray hydrogen, blue and turquoise hydrogen involve more realistic processes for reducing greenhouse gas emissions [5,15]. On the other hand, yellow (or purple) hydrogen is produced by water electrolysis, and the necessary energy is obtained from nuclear power plants [14], whereas green hydrogen can be produced by electrolysis using renewable energy sources for the electricity supplied [17]. With green hydrogen, zero carbon emissions are produced, which is in fact the gold standard for hydrogen in the clean energy sector.

Despite this comprehensive classification, it should be mentioned that there may be cases that do not fall entirely under one color, as more than one source can be used to produce hydrogen [15]. At present, the cost of green hydrogen production is still too high to be a real alternative to gray hydrogen production [4,5,18]. In 2019, the cost of hydrogen production from renewable sources is in the range of \$2.6-4.3 kg⁻¹, which is much higher than the cost of hydrogen produced from fossil sources (\$1.3-2 kg⁻¹) (**Figure 1c**) [5,14]. This significant difference is partly due to the fact that the SMR method is well integrated into the ammonia production process, which is very mature at present. Indeed, the largest amount of hydrogen produced is used as a reagent in ammonia synthesis (50%), but also in methanol (10%) and oil recovery and refining (25%)[18].

The International Renewable Energy Agency (IRENA) estimates that the cost of energy produced from renewable sources will become more competitive by 2050 [5]. For instance, Wisneris et al. [19] estimated that wind power will reduce its cost by 37-49% in 2050. Therefore, a dramatic reduction in the cost of green hydrogen production can be expected in the coming years. Hydrogen production by

electrolysis of water could cost about $\$1.38 \text{ kg}^{-1}$ in 2050, about 60% less than the current cost [5,14,20]. The latter cost forecasts have significantly stimulated interest in hydrogen energy in several countries [5,6,15], especially in the transport sector [6,14].

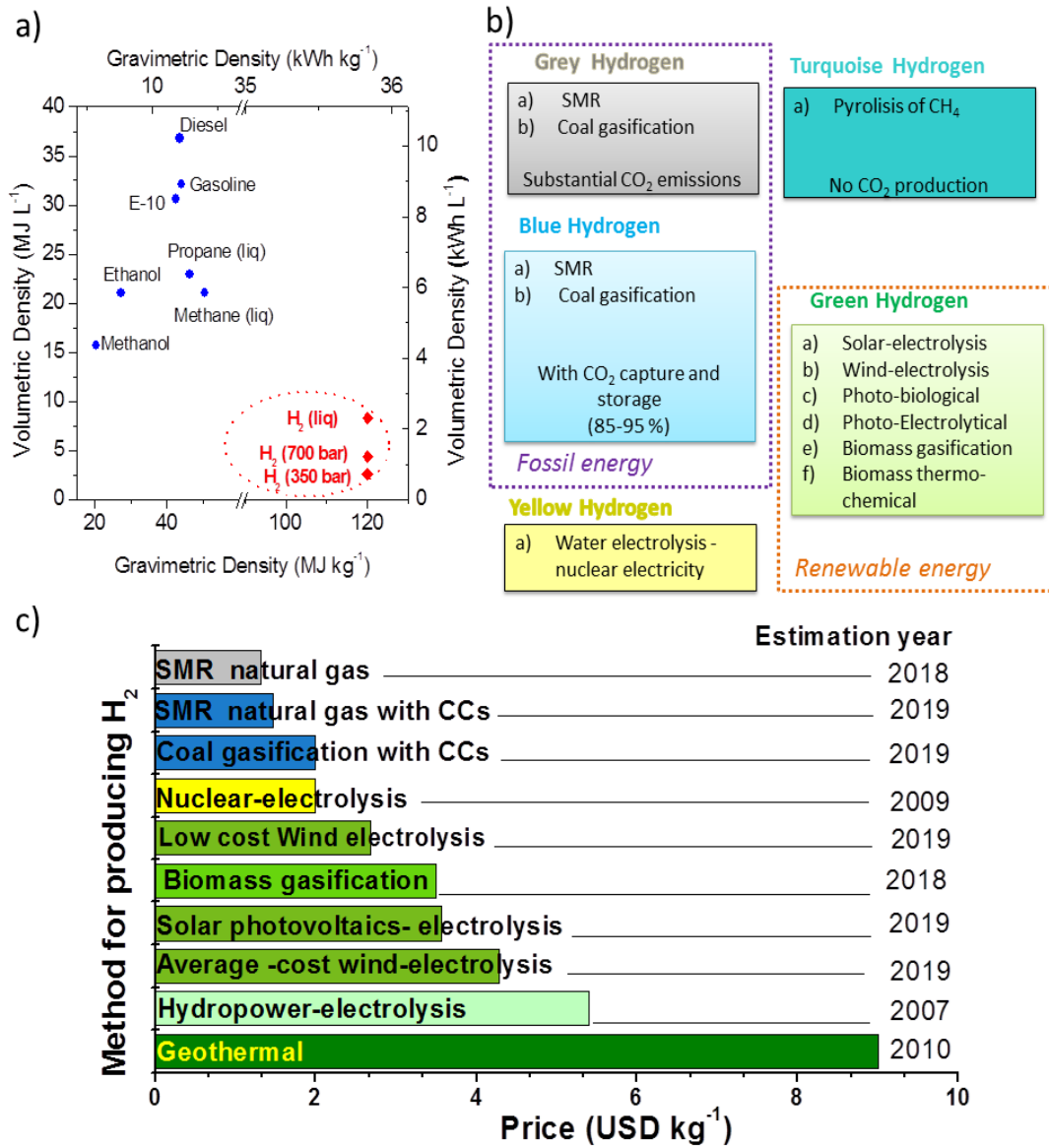


Figure 1. a) Comparison of specific energy (energy per mass or gravimetric density) and energy density (energy per volume or volumetric density) for several fuels based on lower heating values (data recovered from[21]); b) Hydrogen production methods [4,15] ; c) Hydrogen production costs by production source. Literature data obtained from: [5], [12], [10], [11], [13].

Despite significant advances in the design of hydrogen storage systems, hydrogen storage density limits the extensive use of hydrogen in fuel cell vehicles (FCVs). Efforts have focused on increasing the energy density of hydrogen through compression [22–26], liquefaction [27,28], cryo-compression [29,30], and cryo-adsorption at moderate pressures [31–33]. In this study, we compare these different hydrogen storage options with a focus on hydrogen storage by cryo-adsorption on high surface area porous materials, particularly activated carbons, hyper-crosslinked polymers and metal organic frameworks. Recently, significant progress has been made in the characterization and optimization of these systems, which are reviewed in this manuscript. We also provide not only hydrogen storage capacities but hydrogen release capacities considering hydrogen discharge from 10 MPa to 0.5 MPa.

2. Hydrogen storage methods

As stated earlier, the development of the hydrogen supply chain is hampered by its low volumetric energy density, which is a major drawback, especially for automotive applications. For example, a volume of 61.45 m³ would be needed to store 5 kg of hydrogen at 298 K and 0.1 MPa to cover a distance of 500 km. In comparison, a volume of gasoline of about 0.040 m³ is used to cover the same distance with internal combustion engine vehicles. In order to enable the global commercialization of hydrogen FCVs, the U.S. Department of Energy (DOE) has set a series of targets for hydrogen storage systems to achieve in order to become competitive with gasoline hybrid vehicles. **Table 1** shows the current technical targets for hydrogen storage systems in light-duty FCVs, recommended by the DOE [34] and updated in 2017. It should be noted that these targets take into account the weight of the entire storage system, which includes tank, equipment, valves, regulators, piping, mounting brackets and insulation. In addition, they must be achieved in the temperature range of 233-333 K. Furthermore, the hydrogen vehicle is considered to have a useful life of 15 years, during which it is parked in direct sunlight at an average temperature of 308 K.

There are several approaches to increase the volumetric energy density of hydrogen, which are classified into two main groups: (i) material-based methods and; (ii) physical methods (**Figure 2a**). On the one hand, material-based methods are based on the interaction of hydrogen molecules with other compounds, through chemical or physical interactions (*e.g.*, metal hydrides, metal organic frameworks (MOFs), nanostructured carbons, hyper-crosslinked polymers (HCPs)). On the other hand, physical methods consist in reducing the volume occupied by hydrogen molecules by modifying thermodynamic properties such as temperature and pressure.

Table 1. Technical system targets for hydrogen storage in light-duty fuel cell vehicles recommended by the U.S. Department of Energy (DOE) (adapted from [34]).

Storage Parameter	Units	2020	2025	Ultimate
Specific energy from H ₂	kWh kg ⁻¹ (wt.% H ₂)	1.5 (4.5%)	1.8 (5.5 %)	2.2 (6.5%)
Usable energy density from H ₂	kWh L ⁻¹ (kg L ⁻¹)	1.0 (0.030)	1.3 (0.040)	1.7 (0.050)
Storage system cost	\$ kWh ⁻¹ net (\$ kg ⁻¹ H ₂)	10 (333)	9 (300)	8 (266)
Operating ambient temperature	K	233/333 (sun)	233/333 (sun)	233/333 (sun)
Min/max delivery temperature	K	233/353	233/353	233/353
Operational cycle life (1/4 tank to full)	cycles	1,500	1,500	1,500
Min delivery pressure from storage system	MPa (abs)	0.5	0.5	0.5
Max delivery pressure from storage system	MPa (abs)	1.2	1.2	1.2
Onboard efficiency	%	90	90	90
"Well" to power plant efficiency	%	60	60	60
Dormancy time target (minimum until first release from initial 95% usable capacity)	days	7	10	14
Boil-off loss target (max reduction from initial 95% usable capacity after 30 days)	%	10	10	10

Figure 2b shows the evolution of hydrogen density as a function of system temperature and pressure. At temperatures below the critical point ($T_c = 33 \text{ K}$ for H_2), there is a small region in which hydrogen is in liquid phase (*e.g.* 70.8 kg m^{-3} at 21.2 K and 0.1 MPa). Liquid hydrogen is represented by the solid blue line in the isobars of **Figure 2b**. Moreover, at temperatures above T_c , hydrogen is in the gas phase and has a low density, (*e.g.*, 0.081 kg m^{-3} at 298 K and 0.1 MPa). Therefore, the hydrogen density can be increased by: (i) compression in gas cylinders, (ii) liquefaction in cryogenic tanks and (iii) cryo-compression.

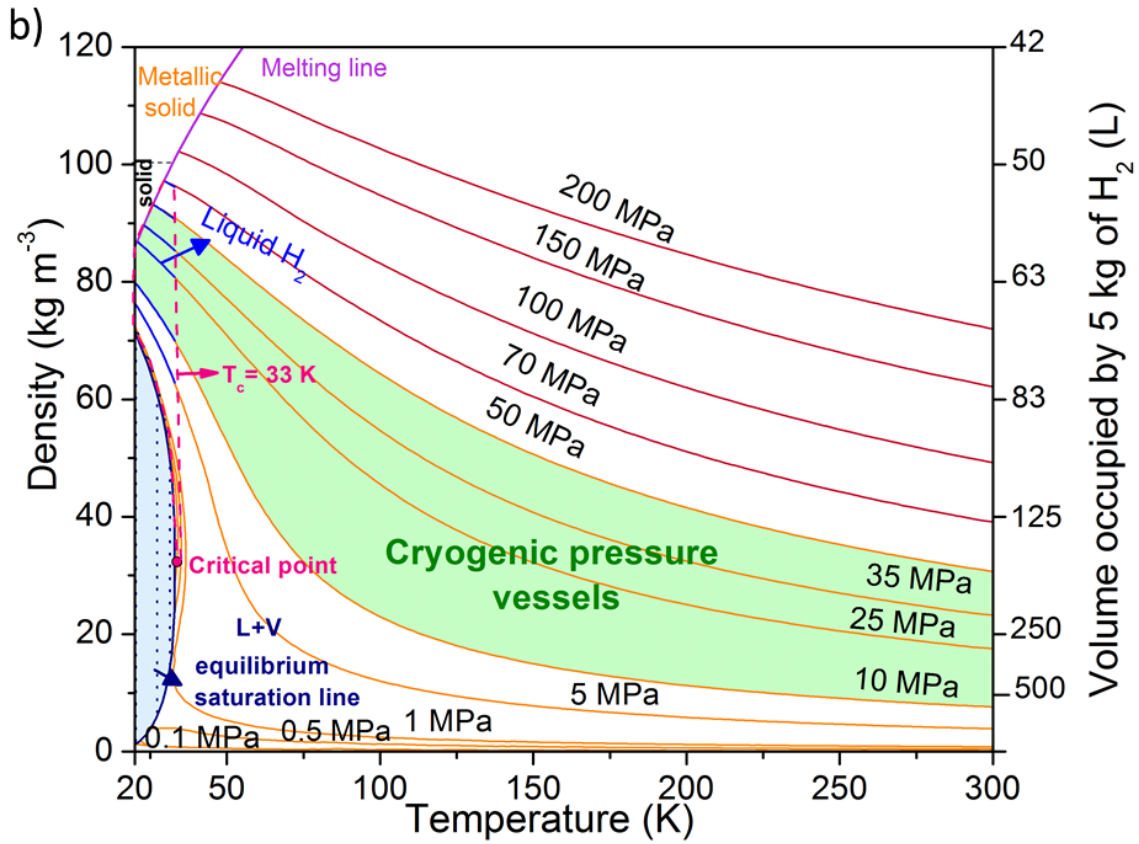
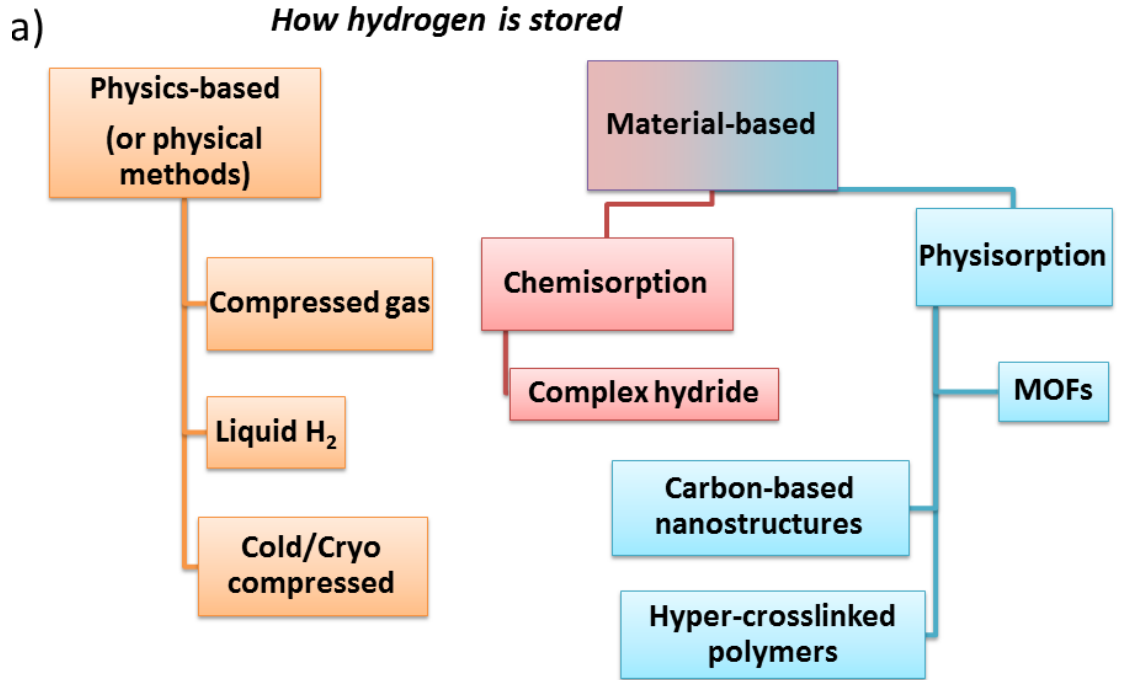


Figure 2. a) Most common ways of storing hydrogen; b) Phase diagram of hydrogen; the density profile was calculated using REFPROP software.

2.1 Hydrogen storage by compression

Compression is the most common method currently used to store hydrogen [35]. Very high pressures, in the range of 20 to 70 MPa, must be used to significantly increase the density of hydrogen [24]. For instance, a density of 42.9 kg m^{-3} at 298 K is achieved by compressing hydrogen to 70 MPa, which is four orders of magnitude higher than the density at ambient conditions, *i.e.*, 0.08 kg m^{-3} at 0.1 MPa and 298 K [18]. In order to withstand such a high level of pressure, suitable materials, designs and safety features must be adopted to ensure the integrity and operation of the tank [22–26]. Indeed, high-pressure tanks are systematically subjected to a rigid protocol of testing and safety regulations before use [36,37].

In order to ensure the long-term integrity of high-pressure tanks, careful selection of the materials used is essential. Hydrogen tends to be adsorbed and dissociated on the surface of metals, diffusing into them and causing their embrittlement [38]. Therefore, the main materials well suited for hydrogen storage are austenitic stainless steel and aluminium alloys, both of which are resistant to hyperbaric conditions and prevent the metal from being embrittled by hydrogen molecules [38,39]. For this purpose, four different types of high-pressure tanks are currently used, namely Types I, II, III, and IV (**Figure 3a**) [37].

Type I tanks generally have a volume between 2.5 and 50 L, and are made of metallic materials [23]. However, the use of metals has two major disadvantages, such as the strong tendency to embrittlement by hydrogen molecules and the high weight [26,37]. In contrast, Type II and III tanks are made of composite materials, which allows a considerable reduction in tank weight [23,37]. More

specifically, their high stability is ensured by carbon or synthetic fiber meshes (partial meshes for Type II tanks and full meshes for Type III tanks), as well as by a thin inner metal lining (steel or aluminum), which ensures gas tightness [23]. Finally, Type IV high-pressure tanks are the most commonly used for storing hydrogen at very high pressure. These tanks are made of carbon fiber, so they are lighter than other types of tanks, but more expensive [18]. In addition, a polymer lining is used to prevent leakage (**Figure 3b**). The cost of a Type IV tank has been estimated at about $\$14.75 \text{ kWh}^{-1}$ for a production rate of 500,000 tanks per year [40,41]. This cost should be understood as the cost of storing one kWh of energy as hydrogen. Considering that 1 kg of hydrogen has an energy of $33.33 \text{ kWh kg}^{-1}$ [23], the cost of compressed gas would be $\$491.6 \text{ kg}^{-1}$ ($\$14.75 \text{ kWh}^{-1} \times 33.33 \text{ kWh kg}^{-1}$). We should add to the latter cost that about 15% of the energy of hydrogen is spent to compress it. Therefore, the price of storing hydrogen in an IV tank would be at least $\$565.4 \text{ kg}^{-1}$. This price is higher than that estimated for other storage methods. **Table 2** summarizes the main technical characteristics of the different high-pressure hydrogen tanks currently in use.

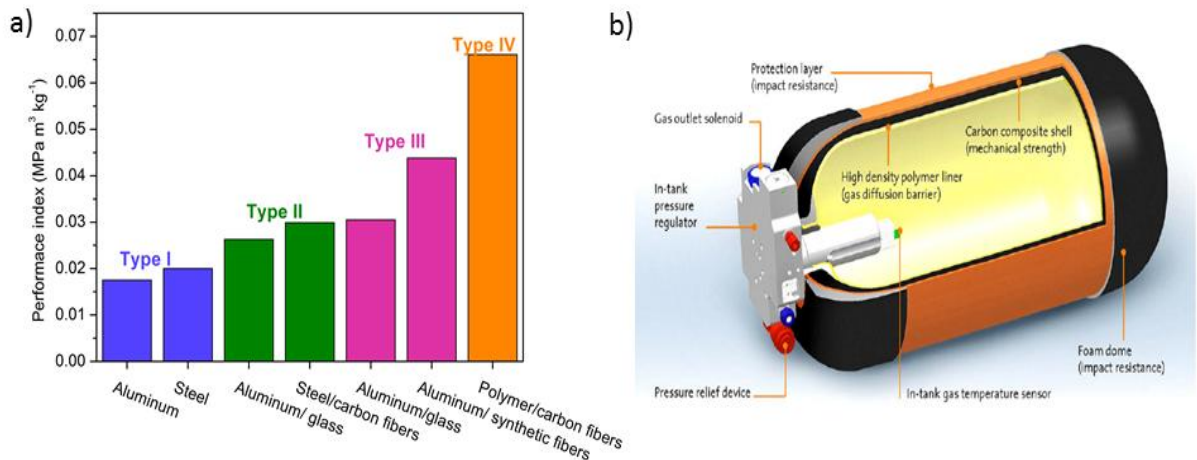


Figure 3. a) Different typologies of high-pressure hydrogen tanks and their performance indexes (adapted from [18]); b) Construction of a typical Type IV pressure tank (reproduced from [42] with permission from Elsevier).

Table 2. Technical features of commercial types I, II, III and IV high-pressure tanks (adapted from [23] and data recovered from [37]).

property	units	Tank type						
		I	I	II ^a	III	III	IV	IV
Net volume	L	2.5	50	50	100	100	36	120
Nominal pressure	bar	200	200/300	300	350	700	350	700
Test pressure	bar	300	300/450	500	525	1050	525	1050
Tank system weight	kg	3.5	58/94	46	48	95	18	84
Tank system volume	L	3.6	60.1/64.7	-	150	150	60	200
H ₂ density at 298 K	kg m ⁻³	14.5	14.5/20.6	20.6	23.3	39.3	23.3	39.3
H ₂ content	kg	0.04	0.72/1.03	1.03	2.33	3.83	0.84	4.65
Grav.H ₂ content	kg H ₂ kg ⁻¹	0.01	0.012/0.011	0.022	0.049	0.041	0.047	0.055
Vol. H ₂ content	kg H ₂ L ⁻¹	0.009	0.012/0.016	0.021	0.016	0.026	0.014	0.023
Grav. energy density	kWh kg ⁻¹	0.333	0.4/0.367	0.73	1.633	1.367	1.567	1.833
Vol. energy density	kWh L ⁻¹	0.3	0.4/0.533	0.70	0.533	0.867	0.467	0.767

^aData recovered from[37]

Compressed hydrogen tanks operate under high stress conditions and require periodic inspections to ensure their safety [43–45]. Although binding legal regulations only require periodic inspections of high-pressure tanks [45], several studies consider the incorporation of continuous structural health monitoring (SHM) systems into high-pressure tanks [43,44,46]. SHM operates by direct feedback of the physical properties of the system (*i.e.*, displacement and temperature), which allows for the determination of other parameters such as distribution of stress, creep or temperature, and detection of leaks [43,47,48]. Therefore, SHM could potentially reduce the weight and costs of the high-pressure tanks [43,49]. Various non-destructive techniques have been considered (*i.e.*, shearography, acoustic emission, vibration monitoring, ultrasonic monitoring, radiography, and thermography) [44,46,47]. The integration of fiber optic sensors into tanks could be a suitable approach for SHM because they have high sensitivity in long-term measurements, resistance to electromagnetic interference, and easy integration into the tank structure [43,49]. In general, fiber optic sensors are permanently attached to

tanks and/or integrated into the composite material structure without influencing its mechanical properties [46,49]. Various optical methods have been investigated for the fabrication of optical sensors, such as visual inspection, digital image correlation (DIC), and fiber Bragg grating (FBG)-based sensing [43,44,47,48].

2.2 Hydrogen storage by liquefaction

Liquid phase hydrogen storage is a physical method that is considered a valid alternative to compression. This method takes advantage of the very high density of liquid hydrogen, namely 70 kg m^{-3} (at 20 K and 0.1 MPa), which is higher than the density of compressed hydrogen gas at 70 MPa (42.6 kg m^{-3}) (**Figure 2b**). This means that a volume of about 13 L is needed to store 1 kg of hydrogen, compared to the 23.3 L used to store 1 kg of hydrogen gas at 70 MPa. The production of liquid hydrogen requires a large amount of energy, which accounts for slightly more than 30% of the chemical energy of hydrogen [50]. This is because the liquefaction of hydrogen is an exothermic process that involves the gradual conversion of ortho-hydrogen, o-H₂, to para-hydrogen, p-H₂ [51]. Therefore, more energy is required than that involved in the phase transition. The theoretical heat of conversion o-H₂ to p-H₂ is indeed 703 kJ kg^{-1} at 20K, which is higher than the heat of vaporization, 446 kJ kg^{-1} . Moreover, the o-H₂ remaining after liquefaction usually evaporates [27,28].

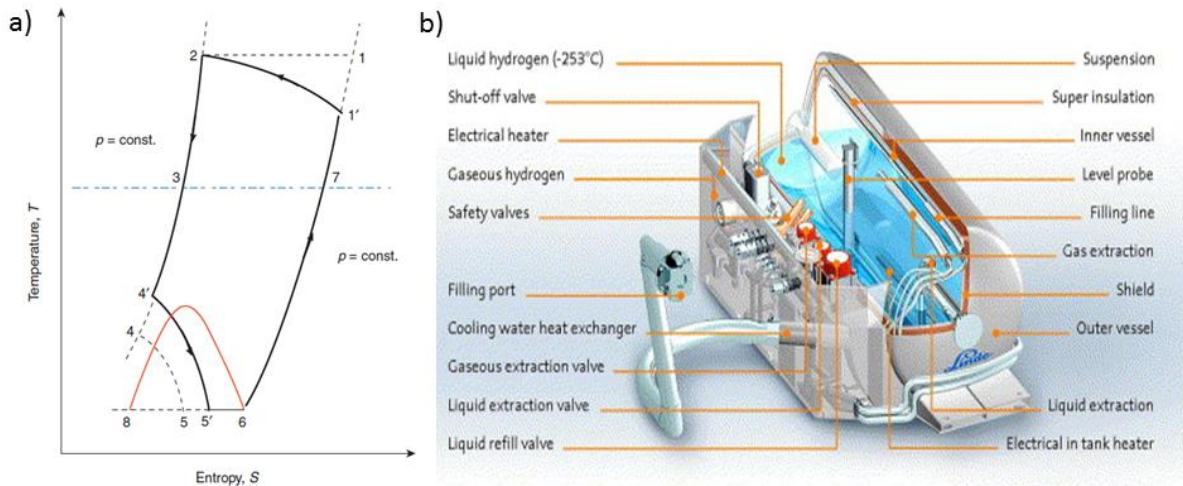


Figure 4.

a) Temperature–entropy diagram for the pre-cooled Linde cycle (reproduced with permission from the Editor[28]); b) Liquid hydrogen storage tank (reproduced with permission from Elsevier [42]).

The first liquefaction of hydrogen was carried out by J. Dewar et al [52]. The authors performed a regenerative cooling process in a double-walled silver glass tank insulated under vacuum [23,28,52]. The most widely used process for liquefying hydrogen is the Joule-Thompson cycle (Linde cycle), which consists of five ideal thermodynamic steps (**Figure 4a**): (i) compression in a high-pressure compressor; (ii) isobaric cooling in a set of heat exchangers and precooling baths; (iii) isenthalpic expansion in a Joule-Thomson expander; (iv) extraction of the cryogenic liquid and; (v) isobaric reheating [28,53,54].

The design of cryogenic liquid hydrogen storage tanks has proven to be a challenge. It is essential to prevent heat transfer as much as possible, in order to minimize hydrogen losses due to evaporation (commonly known as boil off). It has been shown that about 50% of the initial liquid hydrogen evaporates in about 10 days in a standard size static system [28] if the cryogenic tank is not constantly cooled or properly insulated. The rate of hydrogen evaporation from a liquid hydrogen storage tank depends on the size, shape and thermal insulation of the tank [27,55].

A liquid hydrogen storage system consists of an inner tank and an outer tank separated by a vacuum insulation layer, which is filled with several aluminum sheets alternating with glass fibers (**Figure 4b**). Due to the low critical temperature of hydrogen (33K), small amounts of liquefied

hydrogen inevitably evaporate in the tank, increasing the pressure [23,24,27,55]. Therefore, periodic venting procedures are controlled by safety and relief valves. The estimated cost of a liquid hydrogen tank with an internal volume of 100 L is about \$386 kg⁻¹ [56].

2.3 Hydrogen storage by cryo-compression

Cryo-compression combines hydrogen compression and liquefaction, with the benefits and challenges of both storage methods. The density of cryo-compressed hydrogen can be as high as 30-70 kg m⁻³, which is significantly higher than the density of hydrogen at 298 K and 0.1 MPa (**Figure 2b**). Cryo-compression can therefore be used to store 2 to 3 times more hydrogen than in a conventional tank where the hydrogen is compressed at room temperature, *i.e.*, lower pressures are required to store a given amount of hydrogen. Hydrogen cryo-compression meets DOE's 2017 targets, which has spurred the development of cryo-compressed hydrogen storage for automotive applications [29].

A typical cryogenic hydrogen tank consists of an aluminum-lined, carbon-fiber-wrapped inner tank (Type III) and an outer metal shell, comprising a vacuum layer filled with numerous sheets of highly reflective metallized plastic [29,30]. A cryo-compression tank can store 151 L of H₂ and has a total weight (including all accessories) of 187 kg [29]. The second generation of cryo-compression tanks is more compact and lighter than the first. In addition, they are able to store a larger amount of hydrogen, *i.e.*, 10.4 kg compared to 9.3 kg for the first generation. According to some studies, the second generation of cryo-compression tanks can be used on-board, ensuring an autonomy of 800 km [29]. A further reduction in storage volume can be achieved by using third-generation cryo-compression tanks, which are 23% more compact than second-generation tanks [29,57]. The current estimated cost for a cryo-compression hydrogen tank is \$390 kg⁻¹ [56]. Nevertheless, it is not necessary to use materials that

can withstand very high pressures, as is the case for 70 MPa hydrogen tanks. Cryo-compression tanks are therefore lighter than pressurized gas tanks, making them easier to use on-board.

Contrary to cryogenic tanks, cryo-compression tanks are positively affected by boil-off [29,58,59] because it generates pressure that dramatically extends the period of dormancy, as the vehicle is powered by an additional 48 watt-days [29]. In addition, hydrogen cryo-compression can achieve a pressure of 70 MPa, which is necessary for the development of an efficient hydrogen refueling station [30]. The pressure of hydrogen inside a cryo-compressed tank is generally much lower than that reached in pressurized tanks, which minimizes the risk of leakage and is advantageous in terms of safety. However, the low temperatures require continuous monitoring of the thermal insulation of the system, which implies periodic control of the vacuum stability. Cryogenic tanks are not yet able to guarantee vacuum stability for 10 years, which is the greatest technological challenge [60].

2.4 Hydrogen physisorption

Physisorption is a phenomenon that occurs whenever a gas (the adsorptive) is brought into contact with the surface of a solid (the adsorbent) [61]. Physisorption is driven by the fluctuation of Van der Waals interactions between the molecules of the adsorptive and those of the adsorbent [24,62]. The intermolecular interaction between gas and solid molecules consists of both an attractive term, r^{-6} , and a repulsive term, r^{-12} , where r is the distance between the adsorptive molecules and the adsorbent surface [63,64] (**Figure 5a**). Therefore, the total potential energy has a minimum at a distance of about one molecular radius, r_0 , from the adsorbate ($\approx 1.12 r_0$) [38,64,65], corresponding to an adsorption enthalpy of about -1 to -10 kJ mol⁻¹ [27]. The interaction energies involved are low because no chemical bonds are established between the adsorbing molecules and the sorbent surface. Therefore, physisorption is a fully reversible process, which is particularly effective at very low temperatures and moderate pressures

[62]. In the specific case of hydrogen, the density of adsorbed hydrogen increases significantly when the temperature is lowered to 77 K, *i.e.*, the temperature of liquid nitrogen, and can be approximated to the density of liquid hydrogen, *i.e.*, 70 kg m⁻³ [24].

High specific surface area and appropriate pore size distribution are essential textural properties for efficient hydrogen adsorption on porous materials. Remarkable progress has been made in the synthesis of highly porous materials such as zeolites, nanostructured carbons, MOFs and HCPs, among others. The physisorption of hydrogen is particularly enhanced in porous materials with both high microporosity and very narrow pores, *i.e.*, with a pore diameter of 0.6-0.7 nm where there is room for two monolayers of hydrogen, each adsorbed on a pore wall. This is because Van der Waals interactions overlap in narrow pores, resulting in an increased adsorption potential [66,67] (**Figure 5b-c**). According to the BET theory [68], hydrogen molecules can physically adsorb onto a solid surface in infinite layers. Specifically, the enthalpy of adsorption of the first layer is constant and higher than that of the second and upper layers, which corresponds approximately to the enthalpy of condensation. Indeed, the adsorption enthalpy of hydrogen is between -1 and -10 kJ mol⁻¹, while the condensation enthalpy is about -0.9 kJ mol⁻¹. According to these assumptions, if the adsorption temperature is equal to or higher than the boiling temperature of the adsorbent at a given pressure, then a single monolayer is formed [68]. Indeed, the boiling point of hydrogen is 20.6 K, which is much lower than the temperature of liquid nitrogen, 77K.

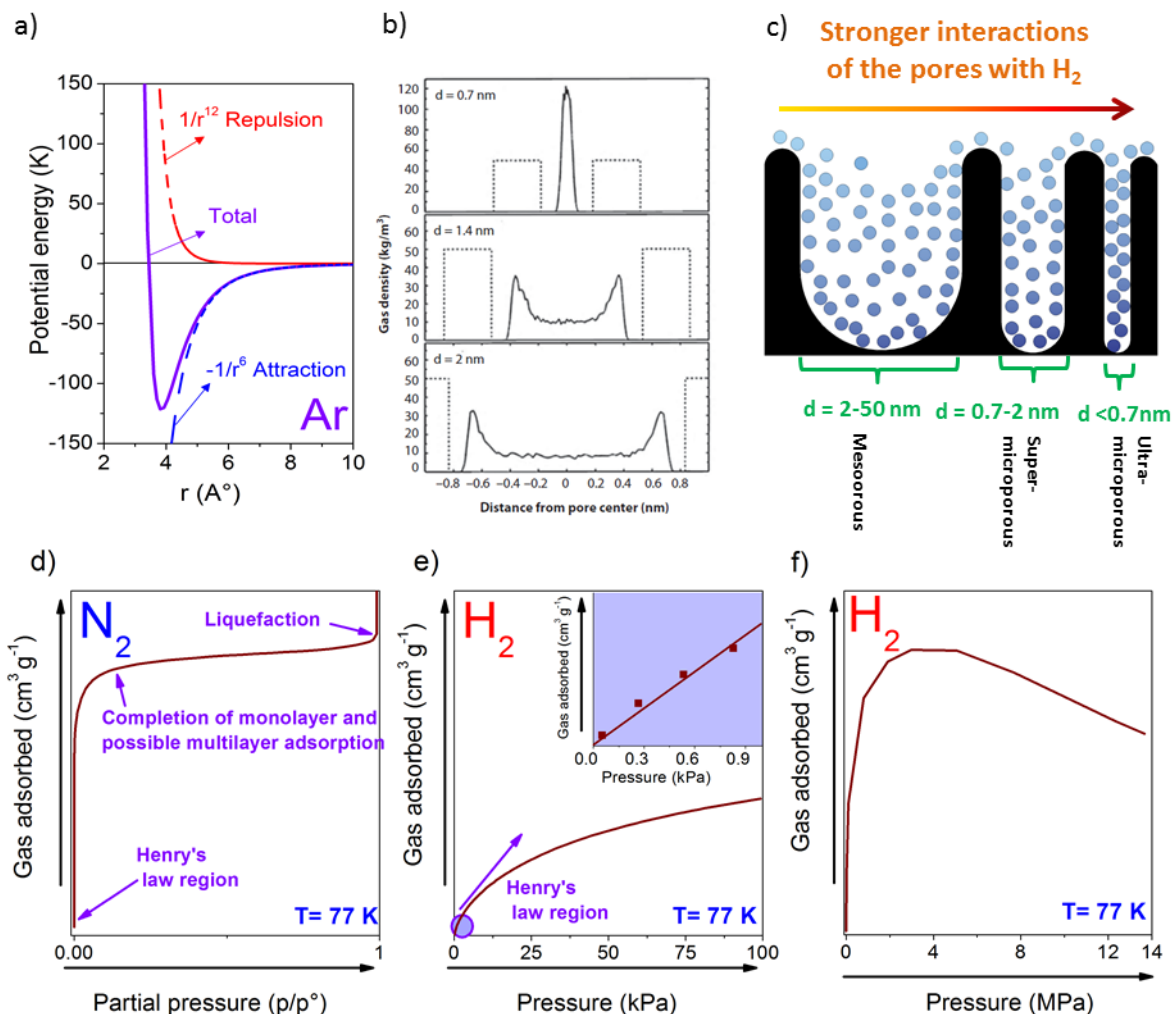


Figure 5 a) Representation of the general shape of an intermolecular potential energy curve for Ar molecules. Parameters for its calculation were taken from [69]; b) Hydrogen density profile inside a slit-shaped pore, at 300 K and 10 MPa, as a function of pore width (reprinted with permission from [70]). Copyright © 2021 American Chemical Society); c) Hydrogen adsorption in pores of different sizes. Adsorption isotherms on a microporous material up to 0.1 MPa of: d) N₂ and e) H₂; f) excess H₂ uptake up to a pressure of 14 MPa.

Figure 5d shows a type I isotherm, according to the IUPAC classification [71], which is usually observed for nitrogen physisorption at 77 K in microporous materials. When hydrogen is adsorbed on the same adsorbent and in the same pressure range at 77K, a plateau is not reached because 77 K is higher than the saturation temperature of hydrogen (**Figure 5e**). The Henry’s law region, where the amount of gas adsorbed linearly increases with pressure, can be observed at very low relative pressures (insert in **Figure 5e**) [72,73] and subsequently, a strong deviation from linearity is observed as the

monolayer approaches saturation. A maximum in the hydrogen isotherm is generally observed when studying hydrogen adsorption at pressures above 5 MPa (**Figure 5f**), and can be explained by the significant contribution of the bulk gas density at high pressures. This is because hydrogen is usually measured in manometric devices where the reported absorption refers to excess hydrogen.

Particular attention should be paid when comparing data on hydrogen storage capacities, as these data may refer to excess, absolute or total hydrogen uptakes, depending on the device used for measurement. Indeed, hydrogen uptake can be measured by gravimetric and volumetric devices. Gravimetric devices provide values of absolute hydrogen adsorption, n_{abs} , defined as the amount of gas confined in the volume of the adsorbed layer, V_a , where the density of adsorbed hydrogen is much higher than the density of hydrogen in the bulk gas phase [74]. On the other hand, volumetric devices provide values of excess hydrogen adsorption, n_{exc} , defined as the difference between the hydrogen uptake on the adsorbent surface at a specific temperature and pressure, and the amount that would be present in the same volume and under the same conditions in the absence of adsorption forces. n_{exc} and n_{abs} are linked as follows:

$$n_{exc} = n_{abs} - \rho_g V_a \quad (1)$$

where ρ_g is the density of the bulk gas phase. The density of the adsorbed hydrogen corresponds approximately to the density of the liquid hydrogen in the volume of the adsorbed layer [75]. Away from the pore walls, the hydrogen density is lower, and equal to the density of the gas phase. The hydrogen density profile inside a pore is shown in **Figure 6a**. n_{exc} is represented by zone A, whereas n_{abs} corresponds to the sum of zones A+B. Furthermore, the sum of the amount of free molecules present in the void spaces and the absolute hydrogen adsorption is defined as the total amount of gas in the system (A+B+C).

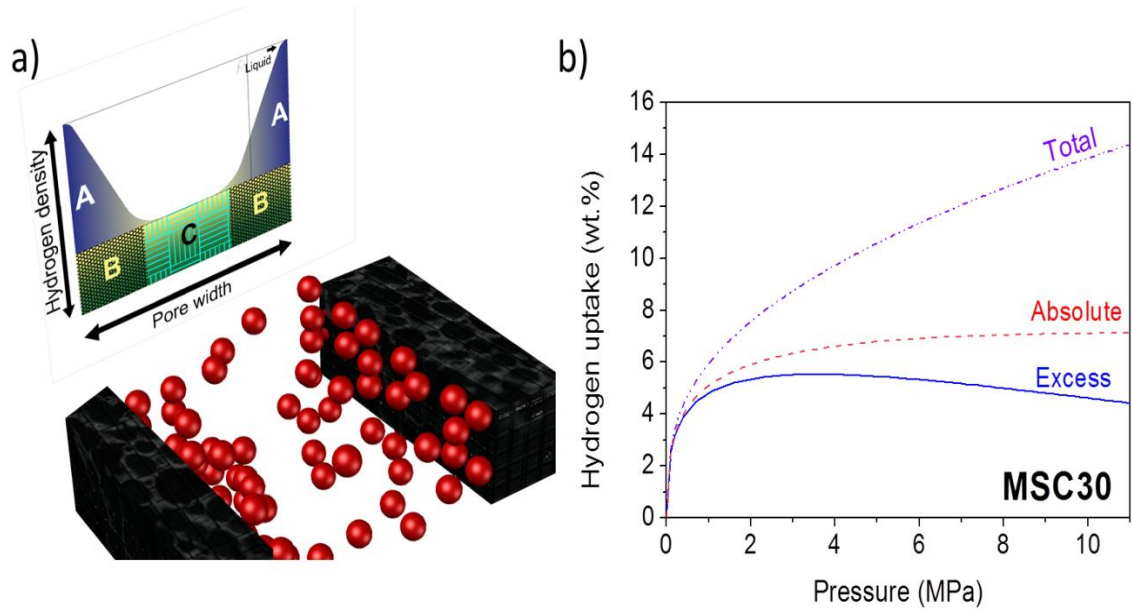


Figure 6. a) Hydrogen density profile in a slit-shaped micropore; and b) Excess, absolute and total hydrogen uptake in the commercial activated carbon MSC30 ($A_{BET} = 3310 \text{ m}^2 \text{ g}^{-1}$, $V_T = 1.60 \text{ cm}^3 \text{ g}^{-1}$ and $V_m = 0.96 \text{ cm}^3 \text{ g}^{-1}$).

An example of the excess, absolute and total adsorption isotherms is given in **Figure 6b** for the commercial activated carbon (CAC) MSC30, which is a highly microporous material (the microporous volume accounts for 60% of the total pore volume). In general, the excess and total amounts are very similar at pressures up to 0.1 MPa. The excess hydrogen adsorption isotherms exhibit a maximum because ρ_g increases significantly at high pressures, while n_{abs} does not increase once it reaches its maximum value at a specific pressure. On the other hand, the total hydrogen uptake is calculated according to Eq. (2), where V_v [$\text{cm}^3 \text{ g}^{-1}$] is the volume of voids in the packing of adsorbent powder:

$$n_{tot} = n_{abs} + \rho_g(V_v - V_a) \quad (2)$$

This expression can be rearranged in Eq. (3) when n_{abs} is substituted by its definition from Eq. (1).

$$n_{tot} = n_{exc} + \rho_g V_v \quad (3)$$

According to Eq. (3), the total adsorption isotherms monotonically increase with ρ_g , thus with pressure.

2.5 Physisorption for hydrogen storage and beyond

A system based on cryo-compression of hydrogen (**Figure 7a**) provides a volume gain of about 22% for the hydrogen storage system compared to a pure compression system. This advantage is particularly marked in the pressure range of 5 to 20 MPa [76]. Although considerable hydrogen storage capacities can be achieved by cryo-compression (*e.g.*, up to 9 wt.% using MOFs [77]), the main shortcoming of this method is the very low operating temperatures required to achieve satisfactory hydrogen storage capacities. Indeed, the DOE targets for hydrogen storage remain difficult to achieve at room temperature in adsorption storage systems. Nevertheless, a cryo-adsorption-based system can be used for non-mechanical hydrogen compression, which is considered a valid alternative to mechanical hydrogen compression technologies used worldwide [22].

Mechanical hydrogen compression, based on conventional piston or diaphragm compression technologies, requires about 15% of the lower heating value (LHV) of hydrogen to provide 0.1 to 70 MPa compression. In addition, mechanical compressors are quite expensive. For example, they account for almost half the price of a hydrogen refueling station [78]. Therefore, electrochemical compressors, based on technology similar to proton-exchange membrane fuel cells, and thermally driven adsorption compressors are likely to solve the above-mentioned drawbacks of mechanical hydrogen compression [18,79,80]. Thermally driven compression of hydrogen by adsorption-desorption (**Figure 7b**) consists of physically adsorbing hydrogen onto a microporous material, which is packed into a previously cooled high-pressure reservoir, *e.g.* at 77 K. By heating the high-pressure reservoir, hydrogen is desorbed, and thus the pressure increases with temperature. The thermally driven compression of hydrogen can be

operated cyclically using two identical tanks in a parallel configuration: while the first tank is cooled to drive hydrogen adsorption, for example using liquid nitrogen, the second is heated to produce hydrogen at high pressure. This technical solution has several advantages over mechanical compressors, such as small size, low maintenance costs due to the absence of moving parts, no noise and vibrations and a favorable energy balance, if industrial waste heat or solar energy is used for heating.

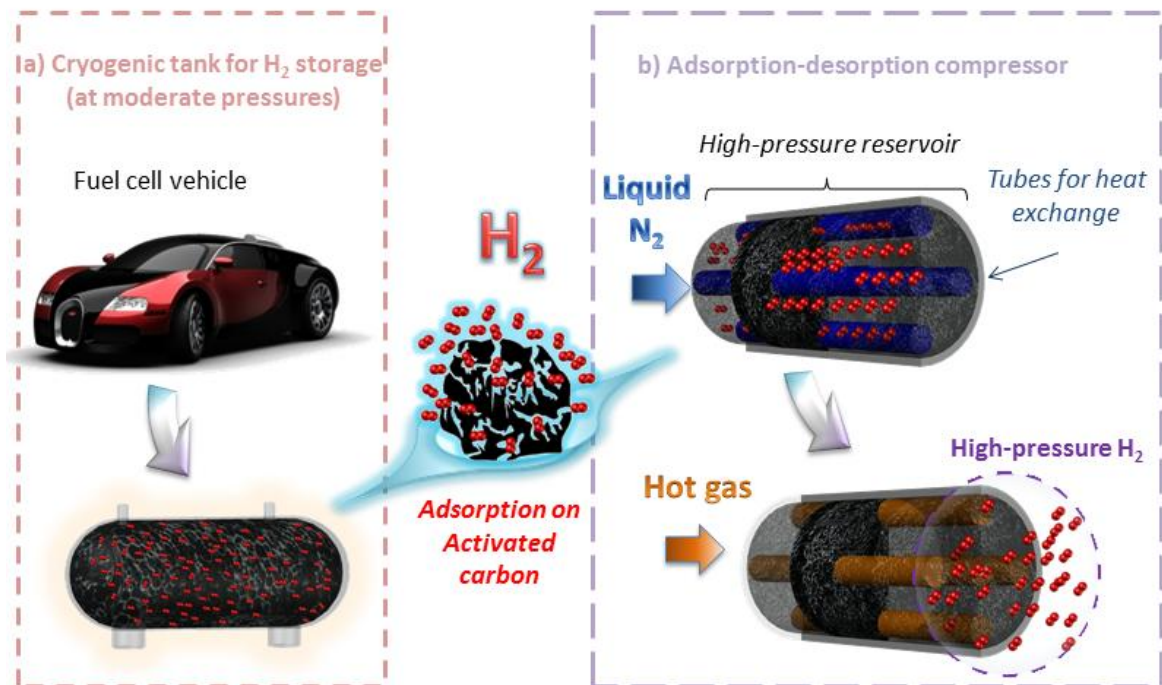


Figure 7. Operating principles of: a) cryogenic tank for H₂ storage; and b) adsorption-desorption compressor.

3. High-surface area porous materials for H₂ physisorption

3.1 Hyper Cross-linked Polymers (HCPs)

High hydrogen storage capacities have been achieved by conducting adsorption on hyper-crosslinked polymers [81]. These materials are made of cheap crosslinked monomers with high porosity and good stability. Currently, Friedel-Crafts alkylation between an external crosslinker and several aromatic monomers is the widely used method for the synthesis of these polymers with a very high

degree of crosslinking (> 40%) [82–89]. Historically, the first HCP was synthesized by Davakov et al.[90] in 1970 using polystyrene as a monomer. Since then, a large variety of HCPs have been synthesized using different monomers [82,88,88,91–93].

To produce HCPs, a linear or slightly branched monomer is stirred in a solvent (usually 1,2-dichloroethane) until it swells (**Figure 8a**). Then, the catalyst and the external crosslinker are added (**Figure 8b**). Lewis acids or protonic acids, such as: AlCl_3 , SnCl_4 , ZnCl_2 , TiCl_4 and FeCl_3 , are used as catalyst for the alkylation process [82,89,94]. It should be emphasized that the appropriate catalyst to be used must match the solvent, especially in terms of steric hindrance and solubility, in order to improve the degree of crosslinking of the HCP produced. [95]. Once the polymerization is complete, the solvent is removed under vacuum (**Figure 8d**), and a rigid network with both a high specific surface area and a high microporosity is obtained (**Figure 8e**) [82,88]. Alternatively, Li et al[96] used a one-step Friedel-Crafts alkylation process to produce HCPs, in which formaldehyde dimethyl ether was used to crosslink several aromatic monomers. Then, naphthalene, anthracene, biphenyl, 1,3,5-triphenylbenzene, phenanthrene were used as precursors [97–99]. The one-step alkylation method has several advantages: (i) inexpensive aromatic monomers such as benzene and cheap solvents can be used; (ii) the process can be scaled up to large production plants and; (iii) the one-step alkylation process is conducted at milder temperatures than the conventional Friedel-Crafts process [89].

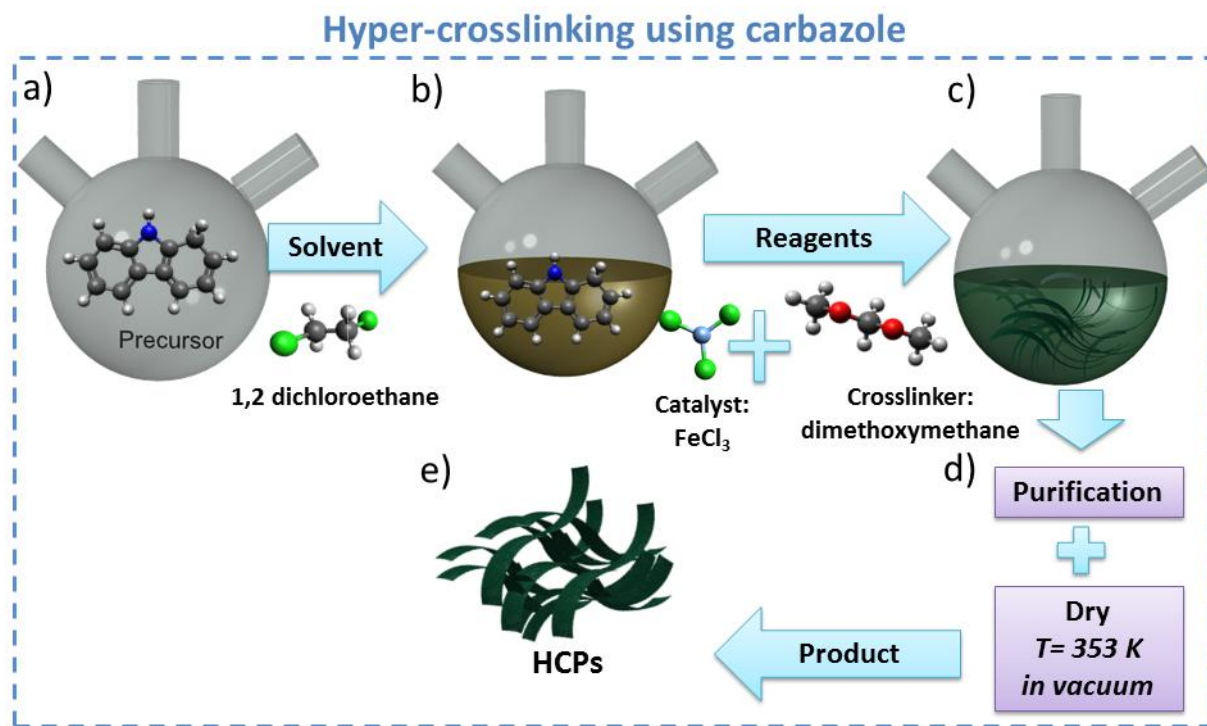


Figure 8. Schematic representation of the hyper-crosslinking synthesis using carbazole as precursor.

HCPs are interesting materials for gas storage and separation because they have very high specific surface area and porosity [85,88,98,100–102]. In addition, it is possible to synthesize HCPs with a high degree of microporosity as well as very narrow pores, which could in principle make them ideal for hydrogen storage in particular [81,103–107]. Hydrogen adsorption capacities in the range of 0.5-1.9 wt.% have been obtained at 77 K and 0.1 MPa using HCPs with very high specific surface areas, up to 1845 m² g⁻¹ [96,105–115]. The most relevant data regarding hydrogen adsorption in HCPs at 77 K and 0.1 MPa have been summarized in **Figure 9a** as well as in **Table S1** and **Table S2**. As expected, higher hydrogen capacities can be obtained at higher pressures [81,116–118]. For instance, an absolute hydrogen uptake of 3.68 wt.% was obtained by Wood et al. at 1.5 MPa and 77 K [104]. **Figure 9b** summarizes the most relevant data on hydrogen storage capacities in HCPs obtained at 77 K and in the pressure range 1-3 MPa.

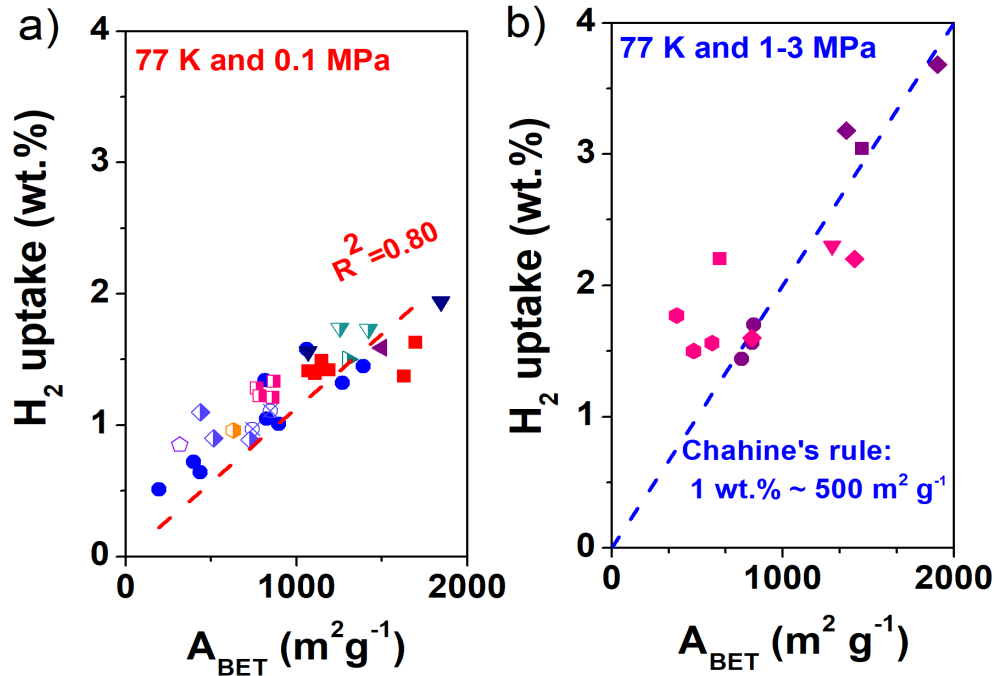


Figure 9. H₂ adsorption on HPCs: a) data reported at 77K and 0.1 MPa in the literature (■ [108], ● [96], ◆ [109], ◀ [105], ▲ [110], ▼ [111], ◐ [106], ◑ [112], ⊗ [113], △ [114], ◊ [107], ◇ [115]); and b) data reported at 77K and 1-1.5 MPa (■ [81], ● [119], ◆ [104], ◇ [116], ● [117], ▼ [118], ◑ [106]). Excess and absolute data are plotted in pink and purple, respectively.

At high pressure and cryogenic temperatures, H₂ adsorption on porous materials follows the so-called Chahine rule [120], which states that H₂ uptake increases at a rate of 1 wt. % per 500 m² g⁻¹ of BET surface area, A_{BET} (blue dashed line in **Figure 9b**). Nevertheless, HCPs with low BET surface area have higher H₂ uptakes than expected with respect to their A_{BET} value according to Chahine's rule (**Figure 9b**). This is due to an underestimation of the specific surface area by the BET theory. Indeed, it is well known that BET theory can underestimate or overestimate the true monolayer loading of the porous solid when N₂ adsorption data are used [71,121–123]. The underestimation of specific surface area is related to the existence of narrow (< 0.7 nm) pores [121,124] where only a monolayer of N₂ is adsorbed and then only a pore wall is taken into account in the A_{BET} determination. In addition, these very narrow pores are not fully accessible to N₂ at 77 K within the set equilibrium times [124,125]. On the other hand, the BET theory overestimates the surface area in materials having large micropores (1 <

$d < 2$ nm) and mesopores ($d \geq 2$ nm), as N_2 uptake proceeds by pore filling and not by monolayer adsorption in these materials [71,121,122,126].

In order to overcome the diffusion problems of N_2 at 77 K in micropores, CO_2 or H_2 isotherms are used [127] and their combination with N_2 or Ar using the 2D-NLDFT-HS model [125,128,129] is adequate for the characterization of carbon materials. However, in the case of HCPs, the use of CO_2 adsorption at 273K for characterization is not suitable as the samples swell in the presence of CO_2 , as reported by Lee et al. [130]. Therefore, the use of the 2D-NLDFT-HS model combining N_2 and H_2 isotherms at 77 K could be advantageous for calculating the textural properties of HCPs. However, to date, kernels for HCPs have not been developed and using those developed for zeolites is not the optimal strategy.

The adsorption properties of HCPs could be improved by the addition of functional nanostructured materials to give nanocomposite HCPs [88,100,101,131–134]. Nanostructured carbon materials, such as multi-walled carbon nanotubes (MWCNTs), graphene oxide (GO) and graphene nanoplatelets (GNPs) have been used in this context [88,133,134]. Castaldo et al. [133] obtained a series of microporous nanocomposites with A_{BET} between 1069 and 1750 $m^2 g^{-1}$ and total pore volumes V_T between 0.28 and 0.54 $cm^3 g^{-1}$ by incorporating MWCNTs into a polymeric matrix composed of divinylbenzene (DVB), styrene (ST), and vinylbenzyl chloride (VBC). After incorporation of MWCNTs, minor changes in A_{BET} (<12 %) were noted but a more significant increase, up to 40 %, in micropore volume was reported, which led to greater H_2 uptake. For instance, the composite with a 40% increase in micropore volume showed an H_2 uptake of 1.4 wt.% at atmospheric pressure and 77 K. The same research team[134] also studied the addition of GO to a polymeric matrix composed of DVB-ST, obtaining materials having A_{BET} between 170 and 1910 $m^2 g^{-1}$ and pore volumes in the range of 0.09-1.35 $cm^3 g^{-1}$. When GO was added, the micropore fraction increased slightly (by 3-14 %) and the total pore volume was reduced (by 10-16

%). This resulted in an increase in H₂ uptake of up to 40 % at 0.1 MPa and 77 K (*e.g.*, from 0.75 to 1.08 wt.% when GO was added). However, the trend described when MWCNTs or GO were incorporated is unclear as the sample panel in each study was limited to 3 for each series [133,134].

Recently, we studied the incorporation of GO into a series of HCPs prepared from four simple and inexpensive molecules: anthracene, benzene, carbazole and dibenzothiophene by the Friedel-Crafts reaction using dimethoxymethane as a crosslinking agent and FeCl₃ as a catalyst [135]. The incorporation of GO was carried out by adding it in the synthesis medium prior to the incorporation of the reagents. The resulting HCPs and HCP-GOs were highly microporous with A_{BET} between 590 and 1120 m² g⁻¹ and pore volumes in the range of 0.39-0.94 cm³ g⁻¹. We obtained textural properties similar to those of materials reported in the literature [88,133,134]; however, the procedure we followed was less time-consuming than that reported in the literature as it was a one-step reaction that did not require prior pre-polymerization[133,134]. Among the samples we obtained, the benzene-derived HCP and its corresponding composite with GO had the highest A_{BET} and were selected to study their H₂ adsorption at 77 K and up to 14 MPa. After H₂ adsorption at pressures above 5 MPa, we found irreversible changes in the porous texture of HCPs and HCP-GO composites that resulted in a progressive decrease in H₂ storage capacity with cycling. These results question the applicability of HCPs and HCP-GO composites for high-pressure hydrogen adsorption, as these systems typically operate in adsorption-desorption cycles from 0.5 MPa to 10 MPa (see **section 5**).

3.2 Activated carbons

Interest in hydrogen adsorption on nanostructured carbon materials was particularly stimulated after the work of Dillon et al. [136], who reported exceptional gravimetric hydrogen adsorption of about 5-10 wt.% at room temperature in single-walled carbon nanotubes (SWCNTs). These values were

refuted by other experiments, which attributed these unusual values to an error in the desorption signal that occurred during temperature-programmed desorption experiments [137]. In addition, Hirscher et al. [138] showed that the hydrogen desorption came from the Ti alloy particles in the sample, introduced during the ultrasonic treatment, rather than from the carbon nanotubes. Despite this, carbon materials were found to be suitable adsorbents for hydrogen adsorption due to their high specific surface areas and the presence of very narrow pores [139,140]. Moreover, carbon materials exhibit other advantages, as they have in most cases: (i) the possibility of being produced from cheap and renewable sources; (ii) high chemical stability; (iii) lower weight than metal hydrides.

The condensation of a hydrogen monolayer on a solid leads to a maximum of $1.32 \cdot 10^{-5}$ mol m⁻² of adsorbed hydrogen. In the case of a graphene sheet with a specific surface area of 2630 m² g⁻¹, considering both sides of the sheet, the maximum theoretical hydrogen uptake is then equal to 6.6 wt.% [141]. Out of all carbon materials, ACs are among those providing the highest hydrogen adsorption capacities [142,143]. The term ACs refers to carbonaceous materials produced by pyrolysis and subsequent, or simultaneous, activation of several precursors: biomass residues [144–146], coal [20,76,147,148] or polymers [81,118], for example. ACs are physico-chemically stable and can have very high surface areas ($A_{\text{BET}} > 1000$ m² g⁻¹), high adsorption capacity and high mechanical strength [149]. The activation process can be driven physically or chemically. On the one hand, physical activation is a two-step process: (i) pyrolysis in the temperature range of 673-1073 K or hydrothermal carbonization (HTC) in the temperature range of 403-478 K, aiming to increase the carbon content [150]; and (ii) partial gasification of the carbon by reaction with an oxidizing gas stream (*e.g.*, water, CO₂) at temperatures between 1000 and 1200 K. On the other hand, chemical activation consists of heat treatment in air (when activating with H₃PO₄ at temperatures below 873 K)[151,152] or under inert gas of the physically mixed or impregnated raw materials with a dehydrating and/or oxidizing agent, such as

alkali hydroxides (NaOH, KOH) [76,153], inorganic acids (H₂SO₄, H₃PO₄) or salts (ZnCl₂) [150]. Chemical activation is generally conducted in the temperature range 673-1173 K [76,150,153]. The final textural and chemical properties of the resulting ACs depend strongly on the synthesis process, the activation time as well as the activation temperature and the activating agent/precursor ratio [76].

Hydrogen adsorption capacities at 298 K and up to 20 MPa are slightly higher than 1 wt.% (**Figure 10a**). Significant improvement can be achieved by storing hydrogen at higher pressures. For example, an adsorption of about 1.5 wt.% can be achieved by increasing the pressure to 35-40 MPa [154]. One way to improve hydrogen adsorption on ACs at room temperature is to functionalize or decorate them with heteroatoms or metal nanoparticles, which enhance the interaction between hydrogen molecules and the carbon surface. Significant effects were obtained at room temperature when studying the hydrogen adsorption on ACs doped with Pd [155]. The addition of metal nanoparticles could also be beneficial due to the spillover phenomenon, *i.e.*, the dissociative chemisorption of molecular hydrogen onto the metal nanoparticles followed by the migration of atomic hydrogen to the carbon surface [156]. In addition, results reported by different authors state that the H₂ uptake is proportional to A_{BET} at 298 K at high pressures (5-20 MPa) [20,76,147,157]. **Figure 10a** shows the excess hydrogen uptake as a function of A_{BET} at different pressure ranges and at 298K. Fairly linear relationships were obtained up to an A_{BET} equal to 2600 m²g⁻¹, the theoretical maximum surface area of carbon materials.

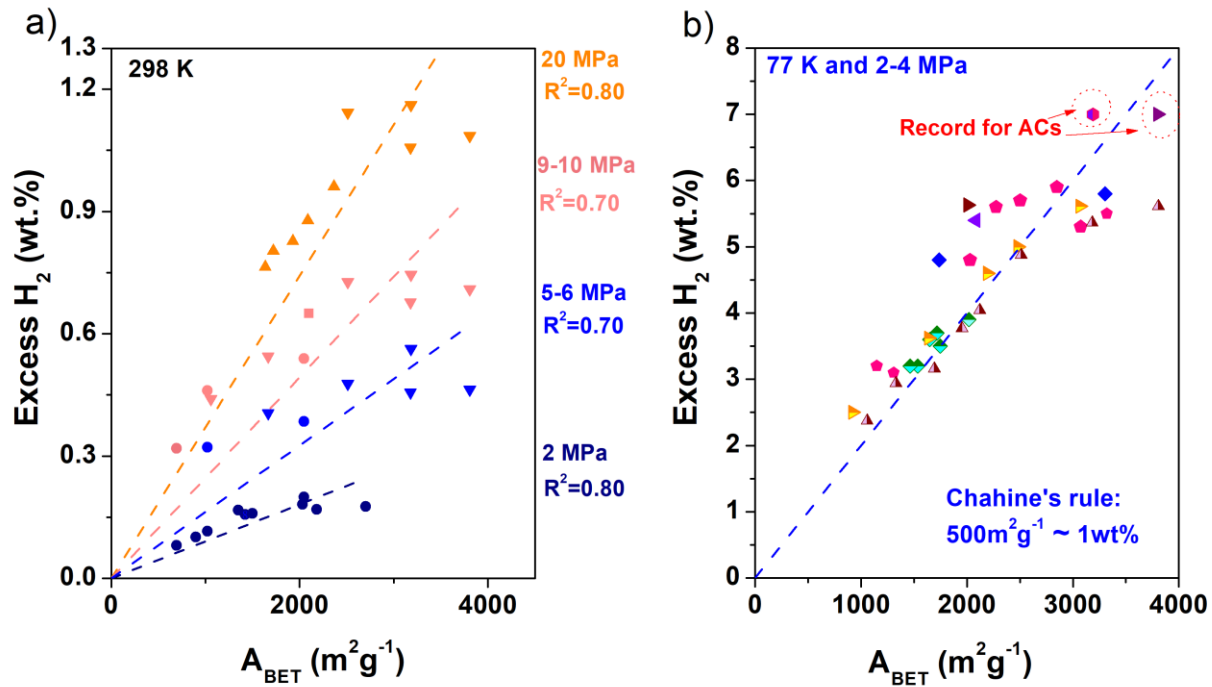


Figure 10. a) Excess hydrogen uptake on ACs reported at 298 K and 2-40 MPa as a function of A_{BET} from recent studies (●[20], ▲[76], ▼[147]). Data obtained at 2, 5-6, 9-10 and 20MPa are displayed in dark blue, blue, pink and orange, respectively); b) Excess hydrogen uptake on ACs reported by recent studies at 77 K and 2-4 MPa (◆ [67], ▼ [158], ▲ [145], ◆ [159], ◆ [157], ▲ [143], ◆ [142]).

Hydrogen adsorption on ACs is significantly improved when the adsorption temperature is decreased to 77 K. At this temperature and at moderate pressures (4 MPa), the amount of hydrogen adsorbed is proportional to A_{BET} and follows Chahine's rule (**Figure 10b**). A hydrogen uptake up to 7 wt.% can be achieved when using ACs with A_{BET} as high as 3000-4000 m^2g^{-1} . As observed for HCPs, ACs having A_{BET} higher than 2600 m^2g^{-1} generally exhibit a lower excess H_2 uptake than expected by Chahine's rule due to the existence of wide pores (> 0.7 nm) that produce an overestimation of the A_{BET} [71,121,122,126]. Furthermore, the surface of ACs can be better described using the 2D-NLDFT-HS model combining the adsorption data of $\text{N}_2 + \text{CO}_2$, $S_{\text{NLDFT N}_2+\text{CO}_2}$, [122] or $\text{N}_2 + \text{H}_2$, $S_{\text{NLDFT N}_2+\text{H}_2}$ [125]. Indeed, in fitting H_2 uptake at high pressures and cryogenic temperatures with specific surface area, better fits were obtained with $S_{\text{NLDFT N}_2+\text{CO}_2}$ than with A_{BET} [67,160]. We have shown that excess

hydrogen adsorption increases by 1.25 wt.% per $500 \text{ m}^2 \text{ g}^{-1}$ of $S_{\text{NLDFT N}_2+\text{CO}_2}$ at 77 K [160]. Although N_2+H_2 adsorption on ACs is not often used for textural characterization, it should be encouraged as it gives the best assessment of H_2 storage capacities when working with ACs as adsorbents [161].

3.3 Metal Organic Frameworks (MOFs)

MOFs are crystalline materials made of metallic nodes, which can be single atoms or clusters of metals, connected to each other by an organic bridge. Transition metals are commonly used to build up metal complexes, but innovative structures with Al^{3+} [162,163] or Mg^{2+} [67,164,165] as nodes also exist. Furthermore, the MOFs can be assembled from secondary building units (SBUs), which are well-defined molecular complex or clusters entities that can be organic or metal-containing and have simple geometrical shapes[166]. Depending on the metal binding sites, different geometries of the framework can be obtained: linear, T-shaped, tetrahedral, square-planar, square-pyramidal, trigonal-bipyramidal, octahedral, cubic, trigonal-prismatic and pentagonal-bipyramidal (**Figure 11a**). However, distorted geometries can be obtained by changing the ligands and co-ligands [167]. Hence, 1-D, 2-D or 3-D structures can be obtained. The dimensionality of the MOFs is normally linked to their textural properties [168]. The large variety of possible metallic nodes, organic linkers, functional groups and crystallographic arrangements may produce countless possible frameworks [31,168–171]. As proof, more than 20,000 different MOFs have been synthesized in the last decade [162]. **Figure 11b** shows an example of the different frameworks than can be synthesized using $(\text{Zn}_4\text{O}(-\text{CO}_2)_6)$ as a node but different organic linkers. It is worth noting that the framework structure significantly depends on the synthesis process conditions, such as solvent, temperature or crystal grow rate[172]. For instance, in MOFs made from $(\text{Zn}_2(\text{OOC})_4)$ paddle-wheel-shaped SBUs, the solvent molecules usually coordinate with the axial sites of Zn ions but can be removed by heating or outgassing without destroying the MOF structure, thus leading to open metal sites [172,173]. Furthermore, MOF's crystallinity allows for unambiguous

structural determination by X-ray diffraction measurements. This makes it possible to calculate adsorption isotherms, binding energies and transport behavior by computational modelling of static and dynamic interactions of guest molecules in MOF pores [77,174,174–176]. In light of their superior textural properties and versatility, MOFs have attracted noteworthy attention in several fields such as gas storage, separation, catalysis, sensing and drug delivery, among others. The so-called MOF-5, synthesized by Yaghi et al [177], has fostered the investigation of hydrogen storage in MOF materials. Indeed, such a structure can have a very high surface area, up to $2800 \text{ m}^2 \text{ g}^{-1}$. Hydrogen adsorption on MOF-5 was first investigated by Rosi et al. [178], and an uptake of 4.8 wt.% at 77 K and 2 MPa was obtained. In addition to developed textural properties, such as a high surface area and microporosity, the MOF structure has a highly connected network of open channels, facilitating the transport of hydrogen within the pores [179]. Furthermore, it is possible to tune the MOF pore size by either interpenetration or interweaving of frameworks. The former occurs when the frameworks are maximally displaced relative to each other by shifting the second framework exactly half the pore size in the x , y , and z directions. On the other hand, interweaving consists in minimizing the distance between frameworks without any atomic overlap [175]. Grand Canonical Monte Carlo (GCMC) simulations have shown that such methods may produce very narrow pores, which are essential for improving hydrogen storage at 77 K [175]. Balderas-Xicohténcatl et al. [180] proved that MOF interpenetration has a beneficial effect on both gravimetric and volumetric hydrogen storage capacities [181].

Excess hydrogen storage capacities in the range of 2.4 to 9.05 wt.% have been obtained in MOFs with surface areas up to $6000 \text{ m}^2 \text{ g}^{-1}$ (**Figure 12a**). To date, the highest excess hydrogen uptake in MOFs, *i.e.*, 9.05 wt.% at 77 K and 7 MPa, has been obtained using the NU-100 framework (Northwestern University) [77].

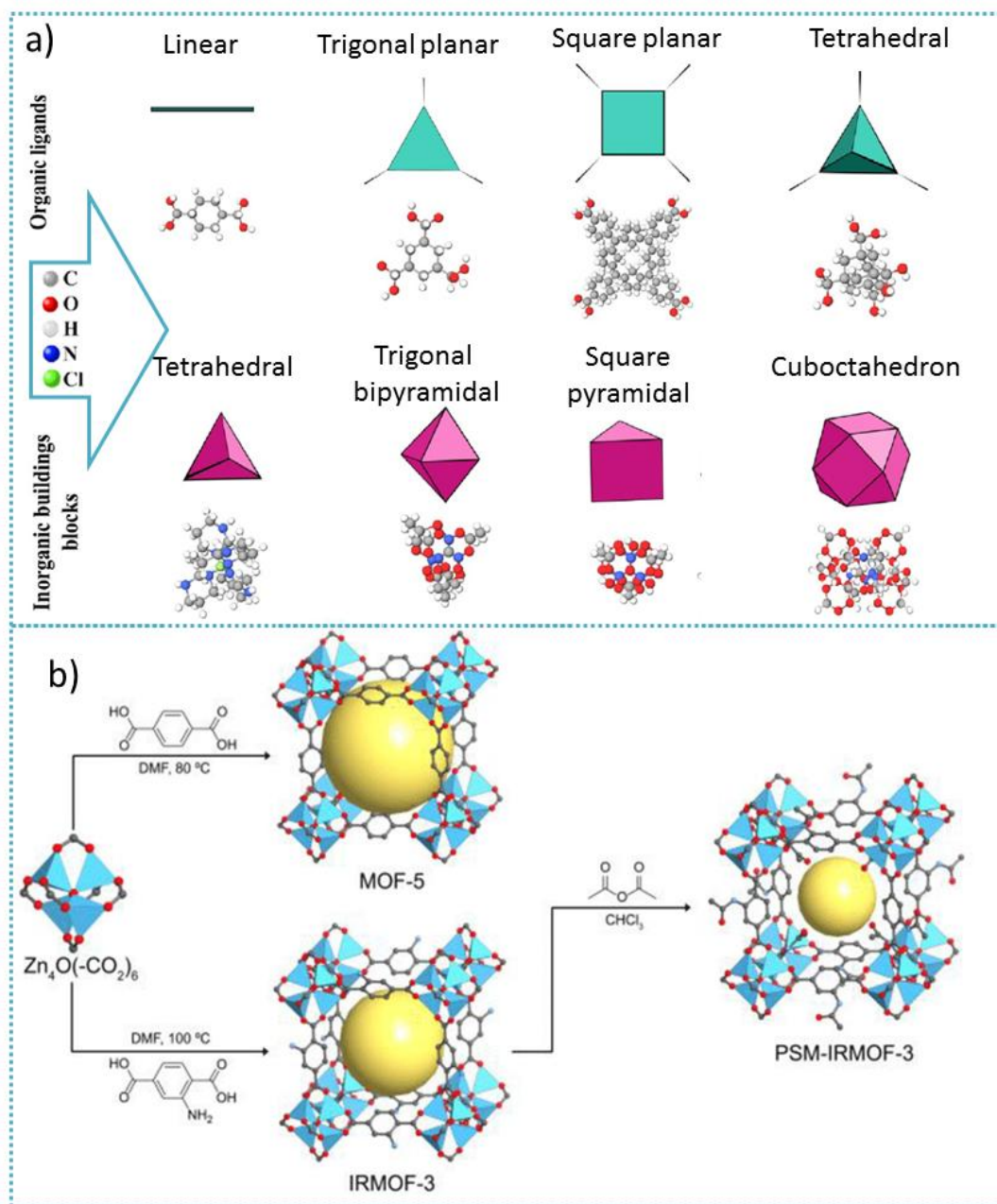


Figure 11. a) Classes of inorganic coordination of MOFs and their geometry (adapted with permission from Elsevier [182]); b) Synthesis pathway of MOF-5, IRMOF-3 and PSM-IRMOF-3. Yellow spheres represent the frameworks' free spaces and have no chemical meaning. Atom colors: Zn, blue tetrahedra; C, gray; O, red; and N, blue. H atoms are omitted for clarity (reprinted with permission from [183]. Copyright © 2021 American Chemical Society).

Isosteric heats of hydrogen adsorption between 3.7 and 6.5 kJ mol^{-1} were obtained for MOF materials (**Figure 12b**). According to the data reported in the open literature (**Figure 12b**), the isosteric

heat of adsorption decreases linearly as the average pore diameter increases ($R^2 = 0.70$). Indeed, higher adsorption forces are produced when hydrogen is adsorbed in very narrow pores, due to the overlapping Van der Waals forces there. Gomez-Gualdron et al. [184] found a linear relationship between specific surface area and pore volume in characterizing several isorecticular zirconium-based MOFs. The same behavior, shown in **Figure 12c**, was also confirmed by using different kinds of MOFs [32,180]. **Figure 12d** gathers volumetric and gravimetric hydrogen uptake on MOFs reported in recent years. More detailed information is available in the **Table S9**. When absolute uptakes were not reported, they were calculated from excess data by using Eq. (1). The temperature and pressure dependency of hydrogen gas density was evaluated with REFPROP software, and V_a was considered equal to the total pore volume. On the other hand, the volumetric hydrogen uptake was calculated by using both the tapped density (**Table S10**) and the crystal density (**Figure 12d** and **Table S9**). It is interesting to note that the tapped density gives a more realistic estimate as it takes into account the particle volume and interparticle void, but it is rarely reported. Conversely, the crystal density of materials can be determined by XRD analysis and is generally reported in the literature [32,33,185]. In MOFs with high BET areas, the hydrogen uptake in volumetric basis reaches a plateau when plotted against the uptake in gravimetric basis (**Figure 12d**). This behavior is well described by the following equation, proposed by Balderas-Xicohténcatl et al [180]:

$$n_v = \frac{n_g}{\frac{a}{k} n_g + V_0} \quad (4)$$

where a , k and V_0 are model parameters. The equation was obtained at 77 K and in the pressure range 2-2.5 MPa using data from several MOFs [180]. It should be noted that the model is in perfect agreement with the experimental data when crystal density is used. Therefore, MOFs having high A_{BET} and high absolute hydrogen uptake on a gravimetric basis are not necessary those that offer the highest hydrogen

uptake on a volumetric basis. Indeed, the balance between volumetric and gravimetric hydrogen adsorption is crucial in the design of a suitable on-board hydrogen storage system [33,180,185]. Optimal gravimetric and volumetric adsorption ensures that storage is not prohibitive in terms of tank weight and volume[32,185].

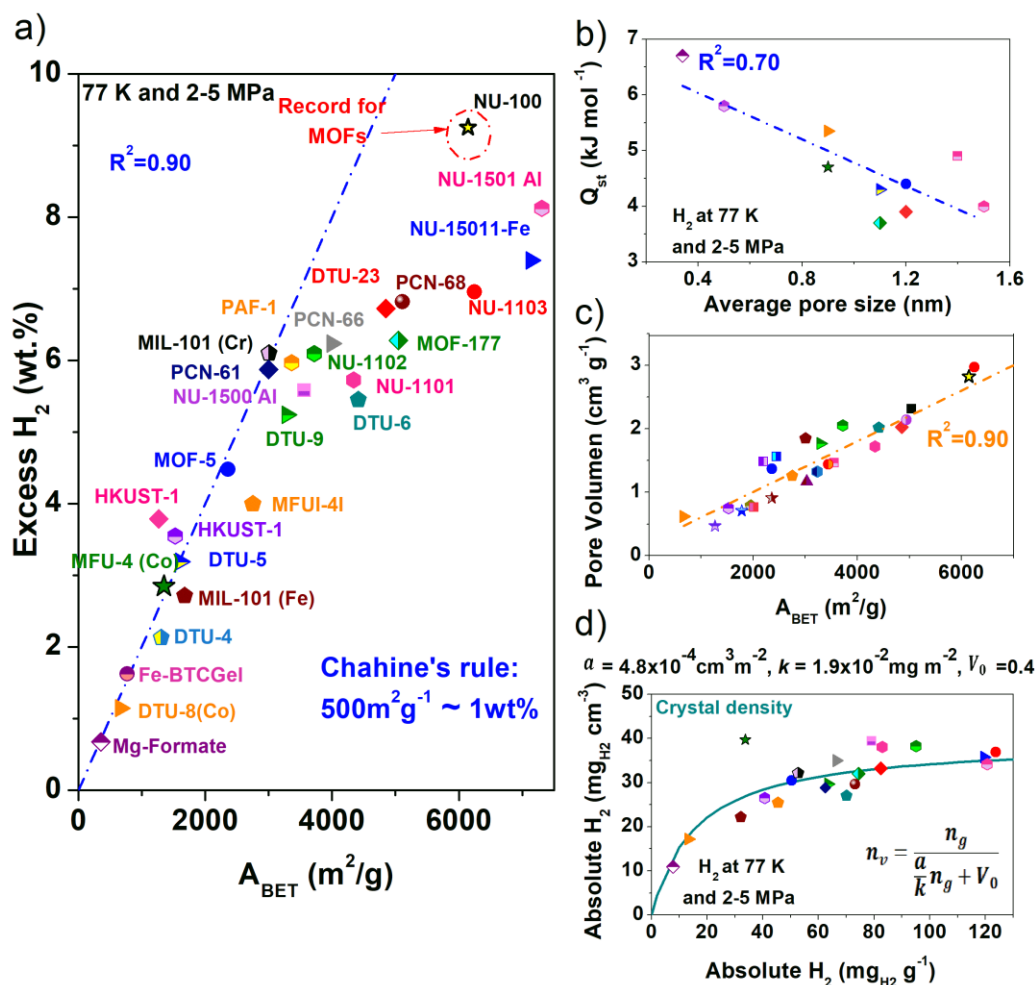


Figure 12. Absolute H_2 uptake at 77 K and 2-7 MPa on metal organic frameworks (MOFs) reported in recent studies ([186], ([187], ([185], ([33], ([77], ([188], ([32], ([189]. a) Chahine's rule in MOFs; b) Isothermic heat of adsorption Q_{st} as function of average pore size; c) Evolution of pore volume with BET area; d) Volumetric versus gravimetric absolute hydrogen uptake of porous materials using the density of the single-crystal for its calculation for MOFs: ([186], ([187], ([185], ([33], ([77], ([188]. The green line in (d) corresponds to the model proposed by Balderas-Xicohténcatl et al in [180]. The absolute uptake from the excess reported data was calculated using REPROF

software to calculate the density of H₂ gas and considering the volume of the adsorbed phase volume to be equal to V_{pore}.

4. Hydrogen release capacities

In a cryo-compression adsorption system, the usable uptake or release capacity (Δn_{H_2}) is defined as the amount of hydrogen released between a maximum tank pressure and a minimum back pressure for use in a fuel cell, for example [33,187,190]. This is commonly calculated using the total adsorption uptake (Eq. 3), as it takes into account the gas compressed in the inter-particle void volume of the adsorbent material [31–33,185,191]. The charging process of a type I high-pressure tank is generally performed at 10 MPa and 77 K [32,33,185,191]. However, some studies have shown that the optimum temperature for the charging process depends on the pore size distribution (PSD) of the adsorbent material [187,192]. For example, Minuto et al. [192] studied the hydrogen release capacity of a series of highly microporous CACs (Nuchar SA-1500, Filtercarb GCC 8x30, and Filtercarb PHA) over a range of 0.1-2 MPa and 77-117 K. They found that the optimal temperatures for Filtercarb GCC 8x30 and PHA were 87 and 107 K, respectively, when the discharge-charge cycles were performed isothermally from 0.1 to 2 MPa.

With regard to back pressure, some authors have considered that it could be as low as 0.2-0.1 MPa [187,192] but recent studies suggest that 0.5 MPa is a more realistic value to consider [31–33]. Indeed, according to some studies, 0.5 MPa is the lower limit for hydrogen flow from a tank to an engine [193]. Furthermore, hydrogen can be discharged by temperature swing desorption, *e.g.*, driven between 77 and 160 K, which can increase the amount hydrogen desorbed compared to an isothermal process (**Figure 13a**). Ahluwalia et al. [194] reported that a temperature swing ($\Delta T = T_{discharge} - T_{charge}$) of 50 K is essential to recover more than 80% of the adsorption capacity on an AC when the charging process is performed at 100 K and 10 MPa and the discharging process is carried out in a range of 0.3 to 0.8 MPa

(and 150 K). Moreover, the Hydrogen Storage Engineering Center of Excellence (HSECoE) [195] proposed to design cryogenic-adsorption pressure tanks considering a charging process driven at 77 K and 10 MPa and a discharge process at 160 K and 0.5MPa.

Figure 13b shows the hydrogen release capacity for MSC30, as a function of the initial temperature and pressure, when discharged at 0.5 MPa and 160 K ($\Delta n_{H_2}^{Ti-160 K}$). The total hydrogen uptake was calculated by using the Modified Dubinin-Astakhov equation (MDA) with the parameters reported in [67] and using Eq.(3). The parameters used and the procedure followed are shown in **Table S11**. The higher the pressure and the lower the temperature during charging, the higher the hydrogen release obtained. **Figure 13c** shows the evolution of $\Delta n_{H_2}^{77K-77K}$ and $\Delta n_{H_2}^{77K-160 K}$ as function of A_{BET} for different MOFs reported in the literature [32,33,77,185,189]. Both release capacities increase linearly with A_{BET} ($R^2 > 0.95$), which is consistent with the fact that the hydrogen uptake of a material is strongly dependent on its textural properties, such as its PSD and specific surface area. For MOFs with surface areas between 681 and 6245 $m^2 g^{-1}$, $\Delta n_{H_2}^{77K-77K}$ is between 1.15 and 10.1 wt.%. These values are significantly increased when the discharge temperature is set to 160 K instead of 77 K ($\Delta n_{H_2}^{77K-160 K}$), as hydrogen release is improved when a temperature swing is performed [194]. $\Delta n_{H_2}^{77K-160K}$ is in the range of 2.6-14 wt.% for MOFs having BET areas of 681 to 7310 $m^2 g^{-1}$.

It is important to note that the release capacities reported in the literature have been calculated using the crystal density, which does not take into account the void volume between the particles and consequently the amount of gas compressed [180,187]. Therefore, calculations using the tapped density lead to higher values of release capacities [31,187] and could be more representative of the real system performance [180,195,196]. The release capacities of MSP20X, MSC30 and MOF-5 were calculated using the MDA parameters and their skeletal and tapped density reported in **Table S11**. By considering

the tapped density instead of the crystal density for the calculation of the MOF-5 release capacities, a value of 12.0 wt.% was obtained for $\Delta n_{\text{H}_2}^{77\text{K}\rightarrow 160\text{K}}$, which is significantly higher than that obtained using the crystal density (7.8 wt.%) (**Table S12** and **Table S11**).

Figure 13d shows the gravimetric release plotted against the volumetric one for various MOFs reported in the literature, and calculated from the crystal density. The volumetric releases $\Delta n_{\text{H}_2}^{77\text{K}\rightarrow 160\text{K}}$ are larger than the volumetric ones in good agreement with the trends observed for gravimetric release capacities. The materials having the largest gravimetric release $\Delta n_{\text{H}_2}^{77\text{K}}$ are not necessary those that offer the largest volumetric $\Delta n_{\text{H}_2}^{77\text{K}}$ in good agreement with the behavior observed for the H₂ absolute uptakes[180]. This is an essential point to consider for a realistic design of hydrogen storage systems.

Figure 13e shows the H₂ stored by: (i) compression at 70 MPa and 298 K, (ii) cryo-compression at 10 MPa and 77 K in an empty tank, and (iii) cryo-adsorption at 10 MPa and 77 K when the system is filled with an adsorbent (MOF-5, MSC30, and the MSP20X). Comparing the systems at 77 K and 10 MPa, it is evident that the contribution of compressed gas to the amount of H₂ stored is lower (blue region in **Figure 13e**) when the tanks are filled with a porous solid, which is related to the reduction in free space of the total tank volume. Furthermore, compared to the empty tank at 77 K and 10 MPa, the total H₂ stored increases by 19, 28 and 35% when MSP20X, MSC30 and MOF-5, respectively, are introduced into the systems, due to the contribution of hydrogen adsorbed in the solids. According to the results displayed in **Figure 13f**, for a discharge at 160 K and 0.5 MPa, at least 95 % of the total storage amount is usable for MSP20X, MSC30, and MOF-5 materials. This corresponds to 17-34 % increases in $\Delta n_{\text{H}_2}^{77\text{K}\rightarrow 160\text{K}}$ compared to that of the empty tank under the same conditions (green area in **Figure 13f**).

Figure 13e shows that the compressed hydrogen accounts for over 63% of the total hydrogen stored by cryogenic adsorption using these 3 porous solids. HCPs were not used in these calculations because they

exhibit irreversible deformation when subjected to pressures above 5 MPa. Finally, compared to hydrogen compression from 0.5 to 70 MPa at 298 K (red dashed line), cryogenic adsorption of hydrogen at 10 MPa on MOF-5 showed a 6% higher release capacity while MSC 30 and MSP20X showed slightly lower release capacities (2 and 8% less, respectively), but at a considerably lower pressure, 10 MPa compared to 70 MPa (**Figure 13f**).

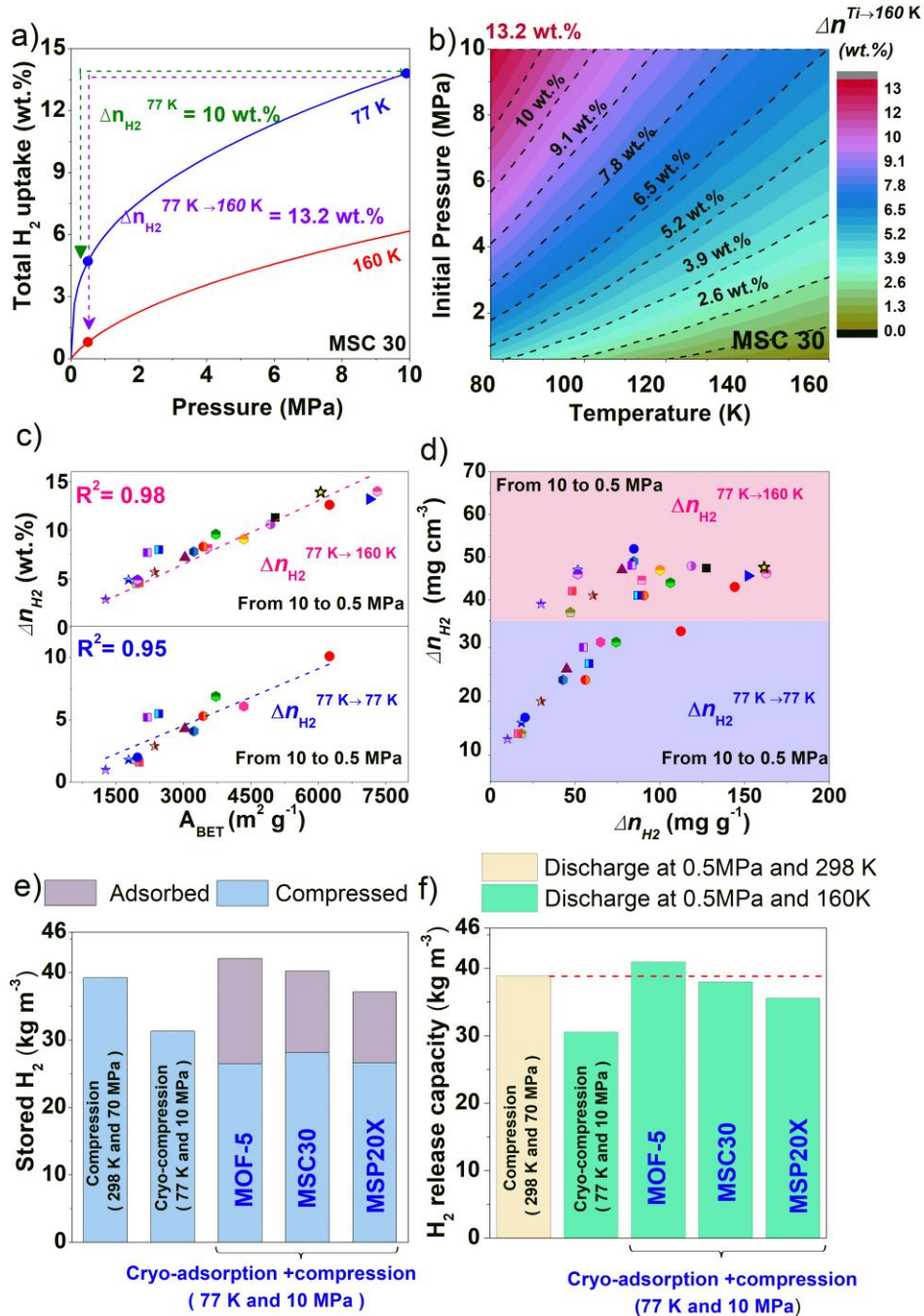


Figure 13. (a) Total H₂ isotherms on the CAC MSC30 at 77 and 160 K up to 10MPa: dashed lines show gravimetric deliverable capacities by decompression (green) and by decompression and heating (purple); (b) Gravimetric deliverable capacity as a function of initial temperature and pressure when the discharge conditions were set to 0.5 MPa and 160 K for the CAC MSC30. Total H₂ uptakes were calculated using the MDA equation and the parameters reported in [67]; (c) Release capacity at 77K, $\Delta n_{H_2}^{77K \rightarrow 77K}$, (bottom), and when heating up from 77 K to 160K, $\Delta n_{H_2}^{77K \rightarrow 160K}$, (top) reported in recent studies: (●) [185], (●) [33], (★) [77], (●) [32], (●) [189] as a function of A_{BET} ; (d) Release capacity at 77K, $\Delta n_{H_2}^{77K \rightarrow 77K}$, (purple region), and when heating up from 77 K to 160K, $\Delta n_{H_2}^{77K \rightarrow 160K}$, (pink region) reported in recent studies in volumetric and gravimetric basis; (e) Storage H₂ by: (i) compression at 70 MPa and 298 K, (ii) cryo-compression at 10 MPa and 77 K in an empty tank, and (iii) cryo-adsorption + compression at 10 MPa and 77 K when

the system is filled with an adsorbent (MOF-5, MSC30, and the MSP20X). In the cryo-adsorption + compression systems the violet region corresponds to the H₂ adsorption contribution; (f) Release capacity of the systems in (e) when decompressing from 10 to 0.5 MPa and heating from 77 K to 160K for the cryo-compression and cryo-adsorption+ adsorption systems, and when decompressing from 70 MPa to 0.5 MPa at 298 K.

5. Conclusions

Among the different approaches to increase hydrogen storage density, cryo-adsorption + compression using high surface area materials has several advantages over other methods because the process is performed (i) at higher temperatures, 77 K, compared to liquefaction systems using temperatures around 20 K, and (ii) at lower pressures, 10-15 MPa, compared to pure compression systems using 70 MPa. Hyper-crosslinked polymers (HCPs), activated carbons (ACs) and MOFs offer high specific surface areas and microporous size distributions that favor hydrogen adsorption, and we critically reviewed the studies available in the open literature. We concluded that, contrary to what has been reported, HCPs cannot be used for hydrogen adsorption at pressures relevant for its storage because they undergo irreversible deformation that gradually decreases their storage capacities and this occurs at pressures above 4 MPa.

Considering a 0.1 m³ (100 L) tank, charged at 77 K and 10 MPa and discharged at 160 K and 0.5 MPa, filled with a high surface area AC, MSC30, or a MOF, MOF-5, the hydrogen release capacities were 38 or 41 kg m⁻³, respectively. Therefore, although having a slightly lower release capacity, MSC30 would be a good, less expensive alternative to MOF-5. Moreover, under these charging-discharging conditions and compared to pure hydrogen compression at 298 K and 70 MPa, MSC30 showed a 2% lower release capacity than pure compression, which is still an attractive option as it would allow the storage pressure to be reduced from 70 to 10 MPa.

Acknowledgements

Pamela Ramirez-Vidal thanks CONACYT-SENER for her scholarship 708651/ 739301. This study was also partly supported by ANR-15-IDEX-04-LUE and TALiSMAN project (2019-000214), funded by ERDF.

References

- [1] Züttel Andreas, Remhof Arndt, Borgschulte Andreas, Friedrichs Oliver. Hydrogen: the future energy carrier. *Philosophical Transactions of the Royal Society A: Mathematical, Physical and Engineering Sciences* 2010;368:3329–42. <https://doi.org/10.1098/rsta.2010.0113>.
- [2] Durbin DJ, Malardier-Jugroot C. Review of hydrogen storage techniques for on board vehicle applications. *International Journal of Hydrogen Energy* 2013;38:14595–617. <https://doi.org/10.1016/j.ijhydene.2013.07.058>.
- [3] Holladay JD, Hu J, King DL, Wang Y. An overview of hydrogen production technologies. *Catalysis Today* 2009;139:244–60. <https://doi.org/10.1016/j.cattod.2008.08.039>.
- [4] Dagdougui H, Sacile R, Bersani C, Ouammi A. Hydrogen Production and Current Technologies. *Hydrogen Infrastructure for Energy Applications*, Elsevier; 2018, p. 7–21. <https://doi.org/10.1016/B978-0-12-812036-1.00002-0>.
- [5] Gielen D, Miranda R, Taibi E. *Hydrogen: A renewable energy perspective*. Tokyo, Japan: 2019.
- [6] *The Future of Hydrogen – Analysis*. IEA n.d. <https://www.iea.org/reports/the-future-of-hydrogen> (accessed January 5, 2021).
- [7] Dincer I. Green methods for hydrogen production. *International Journal of Hydrogen Energy* 2012;37:1954–71. <https://doi.org/10.1016/j.ijhydene.2011.03.173>.
- [8] Hosseini SE, Wahid MA. Hydrogen production from renewable and sustainable energy resources: Promising green energy carrier for clean development. *Renewable and Sustainable Energy Reviews* 2016;57:850–66. <https://doi.org/10.1016/j.rser.2015.12.112>.
- [9] Ausiello A, Micoli L, Turco M, Toscano G, Florio C, Pirozzi D. Biohydrogen production by dark fermentation of *Arundo donax* using a new methodology for selection of H₂-producing bacteria. *International Journal of Hydrogen Energy* 2017;42:30599–612. <https://doi.org/10.1016/j.ijhydene.2017.10.021>.
- [10] Elder R, Allen R. Nuclear heat for hydrogen production: Coupling a very high/high temperature reactor to a hydrogen production plant. *Progress in Nuclear Energy* 2009;51:500–25. <https://doi.org/10.1016/j.pnucene.2008.11.001>.
- [11] Mueller-Langer F, Tzimas E, Kaltschmitt M, Peteves S. Techno-economic assessment of hydrogen production processes for the hydrogen economy for the short and medium term. *International Journal of Hydrogen Energy* 2007;32:3797–810. <https://doi.org/10.1016/j.ijhydene.2007.05.027>.
- [12] Lemus RG, Martínez Duart JM. Updated hydrogen production costs and parities for conventional and renewable technologies. *International Journal of Hydrogen Energy* 2010;35:3929–36. <https://doi.org/10.1016/j.ijhydene.2010.02.034>.
- [13] Salkuyeh YK, Saville BA, MacLean HL. Techno-economic analysis and life cycle assessment of hydrogen production from different biomass gasification processes. *International Journal of Hydrogen Energy* 2018;43:9514–28. <https://doi.org/10.1016/j.ijhydene.2018.04.024>.

- [14] Noussan M, Raimondi PP, Scita R, Hafner M. The Role of Green and Blue Hydrogen in the Energy Transition—A Technological and Geopolitical Perspective. *Sustainability* 2020;13:298. <https://doi.org/10.3390/su13010298>.
- [15] Green hydrogen: A guide to policy making n.d.:52.
- [16] Methane splitting and turquoise ammonia. Ammonia Energy Association n.d. <https://www.ammoniaenergy.org/articles/methane-splitting-and-turquoise-ammonia/> (accessed April 22, 2021).
- [17] Qureshy AMMI, Dincer I. Multi-component modeling and simulation of a new photoelectrochemical reactor design for clean hydrogen production. *Energy* 2021;224:120196. <https://doi.org/10.1016/j.energy.2021.120196>.
- [18] Sdanghi G, Maranzana G, Celzard A, Fierro V. Towards Non-Mechanical Hybrid Hydrogen Compression for Decentralized Hydrogen Facilities. *Energies* 2020;13:3145. <https://doi.org/10.3390/en13123145>.
- [19] Wiser R, Rand J, Seel J, Beiter P, Baker E, Lantz E, et al. Expert elicitation survey predicts 37% to 49% declines in wind energy costs by 2050. *Nat Energy* 2021. <https://doi.org/10.1038/s41560-021-00810-z>.
- [20] Schaefer S, Fierro V, Izquierdo MT, Celzard A. Assessment of hydrogen storage in activated carbons produced from hydrothermally treated organic materials. *International Journal of Hydrogen Energy* 2016;41:12146–56. <https://doi.org/10.1016/j.ijhydene.2016.05.086>.
- [21] Hydrogen Storage. EnergyGov n.d. <https://www.energy.gov/eere/fuelcells/hydrogen-storage> (accessed September 14, 2021).
- [22] Sdanghi G, Maranzana G, Celzard A, Fierro V. Review of the current technologies and performances of hydrogen compression for stationary and automotive applications. *Renewable and Sustainable Energy Reviews* 2019;102:150–70. <https://doi.org/10.1016/j.rser.2018.11.028>.
- [23] Klell M. Storage of Hydrogen in the Pure Form. In: Hirscher M, editor. *Handbook of Hydrogen Storage*, Weinheim, Germany: Wiley-VCH Verlag GmbH & Co. KGaA; 2010, p. 1–37. <https://doi.org/10.1002/9783527629800.ch1>.
- [24] Andersson J, Grönkvist S. Large-scale storage of hydrogen. *International Journal of Hydrogen Energy* 2019;44:11901–19. <https://doi.org/10.1016/j.ijhydene.2019.03.063>.
- [25] Law K, Rosenfeld J. *Cost Analyses of Hydrogen Storage Materials and On-Board Systems*. Cupertino, California: TIAX LLC; 2011.
- [26] Hua T, Ahluwalia R, Peng J-K, Kromer M, Lasher S, McKenney K, et al. *Technical Assessment of Compressed Hydrogen Storage Tank Systems for Automotive Applications*. 2010.
- [27] Züttel A. Hydrogen storage methods. *Naturwissenschaften* 2004;91:157–72. <https://doi.org/10.1007/s00114-004-0516-x>.
- [28] Bonadio L. Fuels– Hydrogen storage | Liquid. In: Garche J, editor. *Encyclopedia of Electrochemical Power Sources*, Amsterdam: Elsevier; 2009, p. 421–39. <https://doi.org/10.1016/B978-044452745-5.00323-3>.

- [29] Aceves SM, Petitpas G, Espinosa-Loza F, Matthews MJ, Ledesma-Orozco E. Safe, long range, inexpensive and rapidly refuelable hydrogen vehicles with cryogenic pressure vessels. *International Journal of Hydrogen Energy* 2013;38:2480–9. <https://doi.org/10.1016/j.ijhydene.2012.11.123>.
- [30] Aceves SM, Espinosa-Loza F, Ledesma-Orozco E, Ross TO, Weisberg AH, Brunner TC, et al. High-density automotive hydrogen storage with cryogenic capable pressure vessels. *International Journal of Hydrogen Energy* 2010;35:1219–26. <https://doi.org/10.1016/j.ijhydene.2009.11.069>.
- [31] Dailly A, Poirier E. Evaluation of an industrial pilot scale densified MOF-177 adsorbent as an on-board hydrogen storage medium. *Energy Environ Sci* 2011;4:3527. <https://doi.org/10.1039/c1ee01426a>.
- [32] García-Holley P, Schweitzer B, Islamoglu T, Liu Y, Lin L, Rodriguez S, et al. Benchmark Study of Hydrogen Storage in Metal–Organic Frameworks under Temperature and Pressure Swing Conditions. *ACS Energy Lett* 2018;3:748–54. <https://doi.org/10.1021/acscenergylett.8b00154>.
- [33] Chen Z, Li P, Anderson R, Wang X, Zhang X, Robison L, et al. Balancing volumetric and gravimetric uptake in highly porous materials for clean energy. *Science* 2020;368:8. <https://doi.org/10.1126/science.aaz8881>.
- [34] DOE Technical Targets for Hydrogen Storage Systems for Material Handling Equipment. EnergyGov n.d. <https://www.energy.gov/eere/fuelcells/doe-technical-targets-hydrogen-storage-systems-material-handling-equipment> (accessed January 7, 2021).
- [35] Amos WA. Costs of Storing and Transporting Hydrogen. 1999. <https://doi.org/10.2172/6574>.
- [36] High-Pressure Hydrogen Tank Testing. EnergyGov n.d. <https://www.energy.gov/eere/fuelcells/high-pressure-hydrogen-tank-testing> (accessed January 13, 2021).
- [37] Krawczak P. Réservoirs haute pression en composites 2002:17.
- [38] Züttel A, Borgschulte A, Schlapbach L, editors. *Hydrogen as a Future Energy Carrier*. 1st edition. Weinheim: Wiley-VCH; 2008.
- [39] Murakami Y. Hydrogen embrittlement. *Metal Fatigue*, Elsevier; 2019, p. 567–607. <https://doi.org/10.1016/B978-0-12-813876-2.00021-2>.
- [40] Rivard E, Trudeau M, Zaghbi K. Hydrogen Storage for Mobility: A Review. *Materials (Basel)* 2019;12. <https://doi.org/10.3390/ma12121973>.
- [41] James BD, Houchins C, Huya-Kouadio JM, DeSantis DA. Final Report: Hydrogen Storage System Cost Analysis. 2016. <https://doi.org/10.2172/1343975>.
- [42] von Helmolt R, Eberle U. Fuel cell vehicles: Status 2007. *Journal of Power Sources* 2007;165:833–43. <https://doi.org/10.1016/j.jpowsour.2006.12.073>.
- [43] Gąsior P, Malesa M, Kaleta J, Kujawińska M, Malowany K, Rybczyński R. Application of complementary optical methods for strain investigation in composite high pressure vessel. *Composite Structures* 2018;203:718–24. <https://doi.org/10.1016/j.compstruct.2018.07.060>.

- [44] Gąsior P, Wachtarczyk K, Błachut A, Kaleta J, Yadav N, Ozga M, et al. Validation of Selected Optical Methods for Assessing Polyethylene (PE) Liners Used in High Pressure Vessels for Hydrogen Storage. *Applied Sciences* 2021;11:5667. <https://doi.org/10.3390/app11125667>.
- [45] Commission Regulation (EU) No 406/2010 of 26 April 2010 implementing Regulation (EC) No 79/2009 of the European Parliament and of the Council on type-approval of hydrogen-powered motor vehicles 2010;406/2010:107.
- [46] Saeter E, Lasn K, Nony F, Echtermeyer AT. Embedded optical fibres for monitoring pressurization and impact of filament wound cylinders. *Composite Structures* 2019;210:608–17. <https://doi.org/10.1016/j.compstruct.2018.11.051>.
- [47] Hao J, Leng J, Wei Z. Non-destructive Evaluation of Composite Pressure Vessel by Using FBG Sensors. *Chinese Journal of Aeronautics* 2007;20:120–3. [https://doi.org/10.1016/S1000-9361\(07\)60017-X](https://doi.org/10.1016/S1000-9361(07)60017-X).
- [48] Degrieck J, Waele WD, Verleysen P. Monitoring of fibre reinforced composites with embedded optical fibre Bragg sensors, with application to filament wound pressure vessels 2001:8.
- [49] Gasior P, Rybczyński R, Kaleta J, Nony F, Villalonga S, Magnier C. High Pressure Composite Vessel With Integrated Optical Fiber Sensors: Monitoring of Manufacturing Process and Operation, 2018. <https://doi.org/10.1115/PVP2018-85157>.
- [50] Sørensen B, Spazzafumo G. 2 - Hydrogen. In: Sørensen B, Spazzafumo G, editors. *Hydrogen and Fuel Cells (Third Edition)*, Academic Press; 2018, p. 5–105. <https://doi.org/10.1016/B978-0-08-100708-2.00002-3>.
- [51] Storage of Pure Hydrogen in Different States. *Hydrogen Storage Technologies*, John Wiley & Sons, Ltd; n.d., p. 97–170. 51
- [52] Dewar J. Preliminary note on the liquefaction of hydrogen and helium. *Proceedings of the Royal Society of London* 1898;63:256–8. <https://doi.org/10.1098/rspl.1898.0031>.
- [53] Starr C. The Design of Hydrogen Liquefiers. *Review of Scientific Instruments* 1941;12:193–8. <https://doi.org/10.1063/1.1769862>.
- [54] Nandi TK, Sarangi S. Performance and optimization of hydrogen liquefaction cycles. *International Journal of Hydrogen Energy* 1993;18:131–9. [https://doi.org/10.1016/0360-3199\(93\)90199-K](https://doi.org/10.1016/0360-3199(93)90199-K).
- [55] Al-Hallaj S, Kiszynski K. Hydrogen Production, Storage and Fuel Cells. In: Al-Hallaj S, Kiszynski K, editors. *Hybrid Hydrogen Systems: Stationary and Transportation Applications*, London: Springer; 2011, p. 31–53. https://doi.org/10.1007/978-1-84628-467-0_3.
- [56] Meneghelli B, Tamburello D, Fesmire J, Swanger A. IV.D.4 Integrated Insulation System for Automotive Cryogenic Storage Tanks 2017:6.
- [57] Petitpas G, Aceves SM, Gupta N. Vehicle refueling with liquid hydrogen thermal compression. *International Journal of Hydrogen Energy* 2012;37:11448–57. <https://doi.org/10.1016/j.ijhydene.2012.04.137>.

- [58] Ahluwalia RK, Peng JK, Roh HS, Hua TQ, Houchins C, James BD. Supercritical cryo-compressed hydrogen storage for fuel cell electric buses. *International Journal of Hydrogen Energy* 2018;43:10215–31. <https://doi.org/10.1016/j.ijhydene.2018.04.113>.
- [59] Ahluwalia RK, Hua TQ, Peng J-K, Lasher S, McKenney K, Sinha J, et al. Technical assessment of cryo-compressed hydrogen storage tank systems for automotive applications. *International Journal of Hydrogen Energy* 2010;35:4171–84. <https://doi.org/10.1016/j.ijhydene.2010.02.074>.
- [60] Hübert T, Boon-Brett L, Buttner W. *Sensors for Safety and Process Control in Hydrogen Technologies*. Boca Raton London New York: Routledge; 2018.
- [61] Thommes M. Physical Adsorption Characterization of Nanoporous Materials. *Chemie Ingenieur Technik* 2010;82:1059–73. <https://doi.org/10.1002/cite.201000064>.
- [62] Züttel A. Materials for hydrogen storage. *Materials Today* 2003;6:24–33. [https://doi.org/10.1016/S1369-7021\(03\)00922-2](https://doi.org/10.1016/S1369-7021(03)00922-2).
- [63] Atkins P, Paula J de. *Atkins' Physical Chemistry*. 10e édition. Oxford ; New York: OUP Oxford; 2014.
- [64] Cabria I, López MJ, Alonso JA. The optimum average nanopore size for hydrogen storage in carbon nanoporous materials. *Carbon* 2007;45:2649–58. <https://doi.org/10.1016/j.carbon.2007.08.003>.
- [65] Cabria I, López MJ, Alonso JA. Simulation of the hydrogen storage in nanoporous carbons with different pore shapes. *International Journal of Hydrogen Energy* 2011;36:10748–59. <https://doi.org/10.1016/j.ijhydene.2011.05.125>.
- [66] Rouquerol F, Rouquerol J, Sing KSW. 2 - Thermodynamics of Adsorption at the Gas/Solid Interface. In: Rouquerol F, Rouquerol J, Sing KSW, Llewellyn P, Maurin G, editors. *Adsorption by Powders and Porous Solids (Second Edition)*, Oxford: Academic Press; 2014, p. 25–56. <https://doi.org/10.1016/B978-0-08-097035-6.00002-4>.
- [67] Sdanghi G, Schaefer S, Maranzana G, Celzard A, Fierro V. Application of the modified Dubinin-Astakhov equation for a better understanding of high-pressure hydrogen adsorption on activated carbons. *International Journal of Hydrogen Energy* 2020;45:25912–26. <https://doi.org/10.1016/j.ijhydene.2019.09.240>.
- [68] Brunauer S, Emmett PH, Teller E. Adsorption of Gases in Multimolecular Layers. *J Am Chem Soc* 1938;60:309–19. <https://doi.org/10.1021/ja01269a023>.
- [69] Smith R, Inomata H, Peters C. Chapter 6 - Equations of State and Formulations for Mixtures. In: Smith R, Inomata H, Peters C, editors. *Supercritical Fluid Science and Technology*, vol. 4, Elsevier; 2013, p. 333–480. <https://doi.org/10.1016/B978-0-444-52215-3.00006-4>.
- [70] Rzepka M, Lamp P, de la Casa-Lillo MA. Physisorption of Hydrogen on Microporous Carbon and Carbon Nanotubes. *J Phys Chem B* 1998;102:10894–8. <https://doi.org/10.1021/jp9829602>.
- [71] Thommes M, Kaneko K, Neimark AV, Olivier JP, Rodriguez-Reinoso F, Rouquerol J, et al. Physisorption of gases, with special reference to the evaluation of surface area and pore size

- distribution (IUPAC Technical Report). *Pure and Applied Chemistry* 2015;87:1051–69. <https://doi.org/10.1515/pac-2014-1117>.
- [72] Do DD, Nicholson D, Do HD. On the Henry constant and isosteric heat at zero loading in gas phase adsorption. *Journal of Colloid and Interface Science* 2008;324:15–24. <https://doi.org/10.1016/j.jcis.2008.05.028>.
- [73] Schindler BJ, LeVan MD. The theoretical maximum isosteric heat of adsorption in the Henry's law region for slit-shaped carbon nanopores. *Carbon* 2008;46:644–8. <https://doi.org/10.1016/j.carbon.2008.01.011>.
- [74] Hurst KE, Gennett T, Adams J, Allendorf MD, Balderas-Xicohténcatl R, Bielewski M, et al. An International Laboratory Comparison Study of Volumetric and Gravimetric Hydrogen Adsorption Measurements. *ChemPhysChem* 2019;20:1997–2009. <https://doi.org/10.1002/cphc.201900166>.
- [75] Sdanghi G, Nicolas V, Mozet K, Maranzana G, Celzard A, Fierro V. Modelling of a hydrogen thermally driven compressor based on cyclic adsorption-desorption on activated carbon. *International Journal of Hydrogen Energy* 2019;44:16811–23. <https://doi.org/10.1016/j.ijhydene.2019.04.233>.
- [76] Fierro V, Zhao W, Izquierdo MT, Aylon E, Celzard A. Adsorption and compression contributions to hydrogen storage in activated anthracites. *International Journal of Hydrogen Energy* 2010;35:9038–45. <https://doi.org/10.1016/j.ijhydene.2010.06.004>.
- [77] Farha OK, Özgür Yazaydın A, Eryazici I, Malliakas CD, Hauser BG, Kanatzidis MG, et al. De novo synthesis of a metal–organic framework material featuring ultrahigh surface area and gas storage capacities. *Nature Chemistry* 2010;2:944.
- [78] Parks G, Boyd R, Cornish J, Remick R. *Hydrogen Station Compression, Storage, and Dispensing Technical Status and Costs* 2014.
- [79] Durmus GNB, Colpan CO, Devrim Y. A review on the development of the electrochemical hydrogen compressors. *Journal of Power Sources* 2021;494:229743. <https://doi.org/10.1016/j.jpowsour.2021.229743>.
- [80] Lototskyy MV, Yartys VA, Pollet BG, Bowman RC. Metal hydride hydrogen compressors: A review. *International Journal of Hydrogen Energy* 2014;39:5818–51. <https://doi.org/10.1016/j.ijhydene.2014.01.158>.
- [81] Lee J-Y, Wood CD, Bradshaw D, Rosseinsky MJ, Cooper AI. Hydrogen adsorption in microporous hypercrosslinked polymers. *Chem Commun* 2006:2670–2. <https://doi.org/10.1039/B604625H>.
- [82] Huang J, Turner SR. Hypercrosslinked Polymers: A Review. *Polymer Reviews* 2018;58:1–41. <https://doi.org/10.1080/15583724.2017.1344703>.
- [83] Dawson R, Stevens LA, Drage TC, Snape CE, Smith MW, Adams DJ, et al. Impact of Water Co-adsorption for Carbon Dioxide Capture in Microporous Polymer Sorbents. *J Am Chem Soc* 2012;134:10741–4. <https://doi.org/10.1021/ja301926h>.
- [84] Dawson R, Ratvijitvech T, Corker M, Laybourn A, Khimyak YZ, Cooper AI, et al. Microporous copolymers for increased gas selectivity. *Polym Chem* 2012;3:2034–8. <https://doi.org/10.1039/C2PY20136D>.

- [85] Saleh M, Lee HM, Kemp KC, Kim KS. Highly Stable CO₂/N₂ and CO₂/CH₄ Selectivity in Hyper-Cross-Linked Heterocyclic Porous Polymers. *ACS Appl Mater Interfaces* 2014;6:7325–33. <https://doi.org/10.1021/am500728q>.
- [86] Jia Z, Wang K, Li T, Tan B, Gu Y. Functionalized hypercrosslinked polymers with knitted N-heterocyclic carbene–copper complexes as efficient and recyclable catalysts for organic transformations. *Catal Sci Technol* 2016;6:4345–55. <https://doi.org/10.1039/C5CY02260F>.
- [87] Song K, Zou Z, Wang D, Tan B, Wang J, Chen J, et al. Microporous Organic Polymers Derived Microporous Carbon Supported Pd Catalysts for Oxygen Reduction Reaction: Impact of Framework and Heteroatom. *J Phys Chem C* 2016;120:2187–97. <https://doi.org/10.1021/acs.jpcc.5b10358>.
- [88] Castaldo R, Gentile G, Avella M, Carfagna C, Ambrogi V. Microporous Hyper-Crosslinked Polystyrenes and Nanocomposites with High Adsorption Properties: A Review. *Polymers* 2017;9:651. <https://doi.org/10.3390/polym9120651>.
- [89] Tan L, Li B, Yang X, Wang W, Tan B. Knitting hypercrosslinked conjugated microporous polymers with external crosslinker. *Polymer* 2015;70:336–42. <https://doi.org/10.1016/j.polymer.2015.06.026>.
- [90] Tsyurupa MP, Davankov VA. Porous structure of hypercrosslinked polystyrene: State-of-the-art mini-review. *Reactive and Functional Polymers* 2006;66:768–79. <https://doi.org/10.1016/j.reactfunctpolym.2005.11.004>.
- [91] Wang X, Mu P, Zhang C, Chen Y, Zeng J, Wang F, et al. Control Synthesis of Tubular Hyper-Cross-Linked Polymers for Highly Porous Carbon Nanotubes. *ACS Appl Mater Interfaces* 2017;9:20779–86. <https://doi.org/10.1021/acsami.7b05345>.
- [92] Cousins K, Zhang R. Highly Porous Organic Polymers for Hydrogen Fuel Storage. *Polymers* 2019;11:690. <https://doi.org/10.3390/polym11040690>.
- [93] Grätz S, Zink S, Krafczyk H, Rose M, Borchardt L. Mechanochemical synthesis of hypercrosslinked polymers: influences on their pore structure and adsorption behaviour for organic vapors. *Beilstein J Org Chem* 2019;15:1154–61. <https://doi.org/10.3762/bjoc.15.112>.
- [94] Sun B, Khan F-A, Süß-Fink G, Therrien B. Chapter 12 - Metal Catalysts Intercalated in Smectite Clays. In: Sadjadi S, editor. *Encapsulated Catalysts*, Academic Press; 2017, p. 387–441. <https://doi.org/10.1016/B978-0-12-803836-9.00012-2>.
- [95] Rueping M, Nachtsheim BJ. A review of new developments in the Friedel–Crafts alkylation – From green chemistry to asymmetric catalysis. *Beilstein J Org Chem* 2010;6. <https://doi.org/10.3762/bjoc.6.6>.
- [96] Li B, Gong R, Wang W, Huang X, Zhang W, Li H, et al. A New Strategy to Microporous Polymers: Knitting Rigid Aromatic Building Blocks by External Cross-Linker. *Macromolecules* 2011;44:2410–4. <https://doi.org/10.1021/ma200630s>.
- [97] Wilson C, Main MJ, Cooper NJ, Briggs ME, Cooper AI, Adams DJ. Swellable functional hypercrosslinked polymer networks for the uptake of chemical warfare agents. *Polym Chem* 2017;8:1914–22. <https://doi.org/10.1039/C7PY00040E>.

- [98] Vinodh R, Hemalatha P, Ganesh M, Peng MM, Abidov A, Palanichamy M, et al. Novel microporous hypercross-linked conjugated quinonoid chromophores with broad light absorption and CO₂ sorption characteristics. *RSC Adv* 2014;4:3678–84. <https://doi.org/10.1039/C3RA45466E>.
- [99] Zhang C, Zhu P-C, Tan L, Liu J-M, Tan B, Yang X-L, et al. Triptycene-Based Hyper-Cross-Linked Polymer Sponge for Gas Storage and Water Treatment. *Macromolecules* 2015;48:8509–14. <https://doi.org/10.1021/acs.macromol.5b02222>.
- [100] Ramezanipour Penchah H, Ghaemi A, Ganadzadeh Gilani H. Benzene-Based Hyper-Cross-Linked Polymer with Enhanced Adsorption Capacity for CO₂ Capture. *Energy Fuels* 2019;33:12578–86. <https://doi.org/10.1021/acs.energyfuels.9b03136>.
- [101] Ramezanipour Penchah H, Ghanadzadeh Gilani H, Ghaemi A. CO₂, N₂, and H₂ Adsorption by Hyper-Cross-Linked Polymers and Their Selectivity Evaluation by Gas–Solid Equilibrium. *J Chem Eng Data* 2020:acs.jced.0c00541. <https://doi.org/10.1021/acs.jced.0c00541>.
- [102] Gao H, Ding L, Bai H, Liu A, Li S, Li L. Pitch-based hyper-cross-linked polymers with high performance for gas adsorption. *J Mater Chem A* 2016;4:16490–8. <https://doi.org/10.1039/C6TA07033G>.
- [103] Germain J, Hradil J, Fréchet JMJ, Svec F. High Surface Area Nanoporous Polymers for Reversible Hydrogen Storage. *Chem Mater* 2006;18:4430–5. <https://doi.org/10.1021/cm061186p>.
- [104] Wood CD, Tan B, Trewin A, Niu H, Bradshaw D, Rosseinsky MJ, et al. Hydrogen Storage in Microporous Hypercrosslinked Organic Polymer Networks. *Chem Mater* 2007;19:2034–48. <https://doi.org/10.1021/cm070356a>.
- [105] Li B, Huang X, Liang L, Tan B. Synthesis of uniform microporous polymer nanoparticles and their applications for hydrogen storage. *J Mater Chem* 2010;20:7444–50. <https://doi.org/10.1039/C0JM01423K>.
- [106] Germain J, Fréchet JMJ, Svec F. Hypercrosslinked polyanilines with nanoporous structure and high surface area: potential adsorbents for hydrogen storage. *J Mater Chem* 2007;17:4989–97. <https://doi.org/10.1039/B711509A>.
- [107] Germain J, Svec F, Fréchet JMJ. Preparation of Size-Selective Nanoporous Polymer Networks of Aromatic Rings: Potential Adsorbents for Hydrogen Storage. *Chem Mater* 2008;20:7069–76. <https://doi.org/10.1021/cm802157r>.
- [108] Germain J, Fréchet JMJ, Svec F. Nanoporous Polymers for Hydrogen Storage. *Small* 2009;5:1098–111. <https://doi.org/10.1002/smll.200801762>.
- [109] Liu G, Wang Y, Shen C, Ju Z, Yuan D. A facile synthesis of microporous organic polymers for efficient gas storage and separation. *J Mater Chem A* 2015;3:3051–8. <https://doi.org/10.1039/C4TA05349D>.
- [110] Li B, Gong R, Luo Y, Tan B. Tailoring the pore size of hypercrosslinked polymers. *Soft Matter* 2011;7:10910–6. <https://doi.org/10.1039/C1SM06113E>.

- [111] Yang X, Yu M, Zhao Y, Zhang C, Wang X, Jiang J-X. Hypercrosslinked microporous polymers based on carbazole for gas storage and separation. *RSC Adv* 2014;4:61051–5. <https://doi.org/10.1039/C4RA09394A>.
- [112] Gu C, Bao Y, Huang W, Liu D, Yang R. Four Simple Structure Carbazole-Based Conjugated Microporous Polymers with Different Soft Connected Chains. *Macromolecular Chemistry and Physics* 2016;217:748–56. <https://doi.org/10.1002/macp.201500420>.
- [113] Luo Y, Zhang S, Ma Y, Wang W, Tan B. Microporous organic polymers synthesized by self-condensation of aromatic hydroxymethyl monomers. *Polym Chem* 2013;4:1126–31. <https://doi.org/10.1039/C2PY20914D>.
- [114] Wang S, Tan L, Zhang C, Hussain I, Tan B. Novel POSS-based organic–inorganic hybrid porous materials by low cost strategies. *J Mater Chem A* 2015;3:6542–8. <https://doi.org/10.1039/C4TA06963C>.
- [115] Luo Y, Li B, Wang W, Wu K, Tan B. Hypercrosslinked Aromatic Heterocyclic Microporous Polymers: A New Class of Highly Selective CO₂ Capturing Materials. *Advanced Materials* 2012;24:5703–7. <https://doi.org/10.1002/adma.201202447>.
- [116] Attia NF, Jung M, Park J, Cho S-Y, Oh H. Facile synthesis of hybrid porous composites and its porous carbon for enhanced H₂ and CH₄ storage. *International Journal of Hydrogen Energy* 2020;45:32797–807. <https://doi.org/10.1016/j.ijhydene.2020.03.004>.
- [117] Park J, Jung M, Jang H, Lee K, Attia NF, Oh H. A facile synthesis tool of nanoporous carbon for promising H₂, CO₂, and CH₄ sorption capacity and selective gas separation. *J Mater Chem A* 2018;6:23087–100. <https://doi.org/10.1039/C8TA08603F>.
- [118] Gatti G, Errahali M, Tei L, Cossi M, Marchese L. On the Gas Storage Properties of 3D Porous Carbons Derived from Hyper-Crosslinked Polymers. *Polymers* 2019;11:588. <https://doi.org/10.3390/polym11040588>.
- [119] McKeown NB, Gahnem B, Msayib KJ, Budd PM, Tattershall CE, Mahmood K, et al. Towards Polymer-Based Hydrogen Storage Materials: Engineering Ultramicroporous Cavities within Polymers of Intrinsic Microporosity. *Angewandte Chemie International Edition* 2006;45:1804–7. <https://doi.org/10.1002/anie.200504241>.
- [120] Poirier E, Chahine R, Bose TK. Hydrogen adsorption in carbon nanostructures. *International Journal of Hydrogen Energy* 2001;26:831–5. [https://doi.org/10.1016/S0360-3199\(01\)00014-3](https://doi.org/10.1016/S0360-3199(01)00014-3).
- [121] Jagiello J, Kenvin J, Celzard A, Fierro V. Enhanced resolution of ultra micropore size determination of biochars and activated carbons by dual gas analysis using N₂ and CO₂ with 2D-NLDFT adsorption models. *Carbon* 2019;144:206–15. <https://doi.org/10.1016/j.carbon.2018.12.028>.
- [122] Jagiello J, Ania C, Parra JB, Cook C. Dual gas analysis of microporous carbons using 2D-NLDFT heterogeneous surface model and combined adsorption data of N₂ and CO₂. *Carbon* 2015;91:330–7. <https://doi.org/10.1016/j.carbon.2015.05.004>.

- [123] Wang TC, Bury W, Gómez-Gualdrón DA, Vermeulen NA, Mondloch JE, Deria P, et al. Ultrahigh Surface Area Zirconium MOFs and Insights into the Applicability of the BET Theory. *J Am Chem Soc* 2015;137:3585–91. <https://doi.org/10.1021/ja512973b>.
- [124] García-Díez E, Schaefer S, Sanchez-Sanchez A, Celzard A, Fierro V, Maroto-Valer MM, et al. Novel Porous Carbons Derived from Coal Tar Rejects: Assessment of the Role of Pore Texture in CO₂ Capture under Realistic Postcombustion Operating Temperatures. *ACS Appl Mater Interfaces* 2019;11:36789–99. <https://doi.org/10.1021/acsami.9b13247>.
- [125] Jagiello J, Kenvin J, Ania CO, Parra JB, Celzard A, Fierro V. Exploiting the adsorption of simple gases O₂ and H₂ with minimal quadrupole moments for the dual gas characterization of nanoporous carbons using 2D-NLDFT models. *Carbon* 2020;160:164–75. <https://doi.org/10.1016/j.carbon.2020.01.013>.
- [126] Gómez-Gualdrón DA, Moghadam PZ, Hupp JT, Farha OK, Snurr RQ. Application of Consistency Criteria To Calculate BET Areas of Micro- And Mesoporous Metal–Organic Frameworks. *J Am Chem Soc* 2016;138:215–24. <https://doi.org/10.1021/jacs.5b10266>.
- [127] Jagiello J, Thommes M. Comparison of DFT characterization methods based on N₂, Ar, CO₂, and H₂ adsorption applied to carbons with various pore size distributions. *Carbon* 2004;42:1227–32. <https://doi.org/10.1016/j.carbon.2004.01.022>.
- [128] Jagiello J, Betz W. Characterization of pore structure of carbon molecular sieves using DFT analysis of Ar and H₂ adsorption data. *Microporous and Mesoporous Materials* 2008;108:117–22. <https://doi.org/10.1016/j.micromeso.2007.03.035>.
- [129] Jagiello J, Ania CO, Parra JB, Jagiello L, Pis JJ. Using DFT analysis of adsorption data of multiple gases including H₂ for the comprehensive characterization of microporous carbons. *Carbon* 2007;45:1066–71. <https://doi.org/10.1016/j.carbon.2006.12.011>.
- [130] Lee J-SM, Briggs ME, Hasell T, Cooper AI. Hyperporous Carbons from Hypercrosslinked Polymers. *Advanced Materials* 2016;28:9804–10. <https://doi.org/10.1002/adma.201603051>.
- [131] Nikoshvili L, Shimanskaya E, Bykov A, Yuranov I, Kiwi-Minsker L, Sulman E. Selective hydrogenation of 2-methyl-3-butyn-2-ol over Pd-nanoparticles stabilized in hypercrosslinked polystyrene: Solvent effect. *Catalysis Today* 2015;241:179–88. <https://doi.org/10.1016/j.cattod.2014.01.045>.
- [132] Bronstein LM, Goerigk G, Kostylev M, Pink M, Khotina IA, Valetsky PM, et al. Structure and Catalytic Properties of Pt-Modified Hyper-Cross-Linked Polystyrene Exhibiting Hierarchical Porosity. *J Phys Chem B* 2004;108:18234–42. <https://doi.org/10.1021/jp046459n>.
- [133] Castaldo R, Avolio R, Cocca M, Gentile G, Errico ME, Avella M, et al. Synthesis and adsorption study of hyper-crosslinked styrene-based nanocomposites containing multi-walled carbon nanotubes. *RSC Adv* 2017;7:6865–74. <https://doi.org/10.1039/C6RA25481K>.
- [134] Castaldo R, Avolio R, Cocca M, Gentile G, Errico ME, Avella M, et al. A Versatile Synthetic Approach toward Hyper-Cross-Linked Styrene-Based Polymers and Nanocomposites. *Macromolecules* 2017;50:4132–43. <https://doi.org/10.1021/acs.macromol.7b00812>.

- [135] Ramirez-Vidal P, Suárez-García F, Canevesi RLS, Castro-Muñiz A, Gadonneix P, Paredes JI, et al. Irreversible deformation of hyper-crosslinked polymers after hydrogen adsorption. *Journal of Colloid and Interface Science* 2022;605:513–27. <https://doi.org/10.1016/j.jcis.2021.07.104>.
- [136] Dillon AC, Jones KM, Bekkedahl TA, Kiang CH, Bethune DS, Heben MJ. Storage of hydrogen in single-walled carbon nanotubes. *Nature* 1997;386:377–9. <https://doi.org/10.1038/386377a0>.
- [137] Konni M, Dadhich AS, Babu Mukkamala S. Impact of surface modifications on hydrogen uptake by Fe@f-MWCNTs and Cu@f-MWCNTs at non-cryogenic temperatures. *International Journal of Hydrogen Energy* 2017;42:953–9. <https://doi.org/10.1016/j.ijhydene.2016.09.085>.
- [138] Hirscher M, Becher M, Haluska M, Dettlaff-Weglikowska U, Quintel A, Duesberg GS, et al. Hydrogen storage in sonicated carbon materials. *Appl Phys A* 2001;72:129–32. <https://doi.org/10.1007/s003390100816>.
- [139] Yushin G, Dash R, Jagiello J, Fischer JE, Gogotsi Y. Carbide-Derived Carbons: Effect of Pore Size on Hydrogen Uptake and Heat of Adsorption. *Advanced Functional Materials* 2006;16:2288–93. <https://doi.org/10.1002/adfm.200500830>.
- [140] López MJ, Cabria I, Alonso JA. Simulated porosity and electronic structure of nanoporous carbons. *J Chem Phys* 2011;135:104706. <https://doi.org/10.1063/1.3633690>.
- [141] Schlapbach L, Züttel A. Hydrogen-storage materials for mobile applications. *Nature* 2001;414:353–8. <https://doi.org/10.1038/35104634>.
- [142] Blankenship II TS, Balahmar N, Mokaya R. Oxygen-rich microporous carbons with exceptional hydrogen storage capacity. *Nat Commun* 2017;8:1545. <https://doi.org/10.1038/s41467-017-01633-x>.
- [143] Wang H, Gao Q, Hu J. High Hydrogen Storage Capacity of Porous Carbons Prepared by Using Activated Carbon. *J Am Chem Soc* 2009;131:7016–22. <https://doi.org/10.1021/ja8083225>.
- [144] Schaefer S, Muñiz G, Izquierdo MT, Mathieu S, Ballinas-Casarrubias ML, González-Sánchez G, et al. Rice straw-based activated carbons doped with SiC for enhanced hydrogen adsorption. *International Journal of Hydrogen Energy* 2017;42:11534–40. <https://doi.org/10.1016/j.ijhydene.2017.02.043>.
- [145] Wróbel-Iwaniec I, Díez N, Gryglewicz G. Chitosan-based highly activated carbons for hydrogen storage. *International Journal of Hydrogen Energy* 2015;40:5788–96. <https://doi.org/10.1016/j.ijhydene.2015.03.034>.
- [146] Choi Y-K, Park S-J. Preparation and characterization of sucrose-based microporous carbons for increasing hydrogen storage. *Journal of Industrial and Engineering Chemistry* 2015;28:32–6. <https://doi.org/10.1016/j.jiec.2015.02.012>.
- [147] Jordá-Beneyto M, Suárez-García F, Lozano-Castelló D, Cazorla-Amorós D, Linares-Solano A. Hydrogen storage on chemically activated carbons and carbon nanomaterials at high pressures. *Carbon* 2007;45:293–303. <https://doi.org/10.1016/j.carbon.2006.09.022>.

- [148] de la Casa-Lillo MA, Lamari-Darkrim F, Cazorla-Amorós D, Linares-Solano A. Hydrogen Storage in Activated Carbons and Activated Carbon Fibers. *J Phys Chem B* 2002;106:10930–4. <https://doi.org/10.1021/jp014543m>.
- [149] Yahya MA, Al-Qodah Z, Ngah CWZ. Agricultural bio-waste materials as potential sustainable precursors used for activated carbon production: A review. *Renewable and Sustainable Energy Reviews* 2015;46:218–35. <https://doi.org/10.1016/j.rser.2015.02.051>.
- [150] Castro-Gutiérrez J, Celzard A, Fierro V. Energy Storage in Supercapacitors: Focus on Tannin-Derived Carbon Electrodes. *Front Mater* 2020;7. <https://doi.org/10.3389/fmats.2020.00217>.
- [151] Vivo-Vilches JF, Celzard A, Fierro V, Devin-Ziegler I, Brosse N, Dufour A, et al. Lignin-Based Carbon Nanofibers as Electrodes for Vanadium Redox Couple Electrochemistry. *Nanomaterials* 2019;9:106. <https://doi.org/10.3390/nano9010106>.
- [152] Montané D, Torné-Fernández V, Fierro V. Activated carbons from lignin: kinetic modeling of the pyrolysis of Kraft lignin activated with phosphoric acid. *Chemical Engineering Journal* 2005;106:1–12. <https://doi.org/10.1016/j.cej.2004.11.001>.
- [153] Melouki R, Llewellyn PL, Tazibet S, Boucheffa Y. Hydrogen adsorption on activated carbons prepared from olive waste: effect of activation conditions on uptakes and adsorption energies. *J Porous Mater* 2017;24:1–11. <https://doi.org/10.1007/s10934-016-0230-z>.
- [154] Voskuilen TG, Pourpoint TL, Dailly AM. Hydrogen adsorption on microporous materials at ambient temperatures and pressures up to 50 MPa. *Adsorption* 2012;18:239–49. <https://doi.org/10.1007/s10450-012-9397-z>.
- [155] Zhao W, Fierro V, Zlotea C, Izquierdo MT, Chevalier-César C, Latroche M, et al. Activated carbons doped with Pd nanoparticles for hydrogen storage. *International Journal of Hydrogen Energy* 2012;37:5072–80. <https://doi.org/10.1016/j.ijhydene.2011.12.058>.
- [156] Schaefer S, Fierro V, Szczurek A, Izquierdo MT, Celzard A. Physisorption, chemisorption and spill-over contributions to hydrogen storage. *International Journal of Hydrogen Energy* 2016;41:17442–52. <https://doi.org/10.1016/j.ijhydene.2016.07.262>.
- [157] Tellez-Juárez MC, Fierro V, Zhao W, Fernández-Huerta N, Izquierdo MT, Reguera E, et al. Hydrogen storage in activated carbons produced from coals of different ranks: Effect of oxygen content. *International Journal of Hydrogen Energy* 2014;39:4996–5002. <https://doi.org/10.1016/j.ijhydene.2014.01.071>.
- [158] Zhao W, Fierro V, Fernández-Huerta N, Izquierdo MT, Celzard A. Hydrogen uptake of high surface area-activated carbons doped with nitrogen. *International Journal of Hydrogen Energy* 2013;38:10453–60. <https://doi.org/10.1016/j.ijhydene.2013.06.048>.
- [159] Fierro V, Szczurek A, Zlotea C, Marêché JF, Izquierdo MT, Albiniak A, et al. Experimental evidence of an upper limit for hydrogen storage at 77K on activated carbons. *Carbon* 2010;48:1902–11. <https://doi.org/10.1016/j.carbon.2010.01.052>.
- [160] Ramirez-Vidal P, Canevesi RLS, Sdanghi G, Schaefer S, Maranzana G, Celzard A, et al. A Step Forward in Understanding the Hydrogen Adsorption and Compression on Activated Carbons. *ACS Appl Mater Interfaces* 2021;13:12562–74. <https://doi.org/10.1021/acsami.0c22192>.

- [161] Sdanghi G, Maranzana G, Celzard A, Fierro V. Hydrogen Adsorption on Nanotextured Carbon Materials. *Hydrogen Storage Technologies*, John Wiley & Sons, Ltd; 2018, p. 263–320. <https://doi.org/10.1002/9781119460572.ch9>.
- [162] Férey G, Latroche M, Serre C, Millange F, Loiseau T, Percheron-Guégan A. Hydrogen adsorption in the nanoporous metal-benzenedicarboxylate $M(\text{OH})(\text{O}_2\text{C}-\text{C}_6\text{H}_4-\text{CO}_2)$ ($M = \text{Al}^{3+}, \text{Cr}^{3+}$), MIL-53. *Chem Commun* 2003;2976–7. <https://doi.org/10.1039/B308903G>.
- [163] Loiseau T, Lecroq L, Volkringer C, Marrot J, Férey G, Haouas M, et al. MIL-96, a Porous Aluminum Trimesate 3D Structure Constructed from a Hexagonal Network of 18-Membered Rings and μ_3 -Oxo-Centered Trinuclear Units. *J Am Chem Soc* 2006;128:10223–30. <https://doi.org/10.1021/ja0621086>.
- [164] Dincă M, Long JR. Strong H_2 Binding and Selective Gas Adsorption within the Microporous Coordination Solid $\text{Mg}_3(\text{O}_2\text{C}-\text{C}_{10}\text{H}_6-\text{CO}_2)_3$. *J Am Chem Soc* 2005;127:9376–7. <https://doi.org/10.1021/ja0523082>.
- [165] Rood JA, Noll BC, Henderson KW. Synthesis, Structural Characterization, Gas Sorption and Guest-Exchange Studies of the Lightweight, Porous Metal–Organic Framework α - $[\text{Mg}_3(\text{O}_2\text{CH})_6]$. *Inorg Chem* 2006;45:5521–8. <https://doi.org/10.1021/ic060543v>.
- [166] Li M, Li D, O’Keeffe M, Yaghi OM. Topological Analysis of Metal–Organic Frameworks with Polytopic Linkers and/or Multiple Building Units and the Minimal Transitivity Principle. *Chem Rev* 2014;114:1343–70. <https://doi.org/10.1021/cr400392k>.
- [167] Lin X, Jia J, Champness NR, Hubberstey P, Schröder M. Metal-organic framework materials for hydrogen storage. *Solid-State Hydrogen Storage*, Elsevier; 2008, p. 288–312. <https://doi.org/10.1533/9781845694944.3.288>.
- [168] Al-Maythaly BA. Metal-organic framework based membranes for gas separation. *Advanced Nanomaterials for Membrane Synthesis and its Applications*, Elsevier; 2019, p. 203–26. <https://doi.org/10.1016/B978-0-12-814503-6.00009-4>.
- [169] Ryu U, Jee S, Rao PC, Shin J, Ko C, Yoon M, et al. Recent advances in process engineering and upcoming applications of metal–organic frameworks. *Coordination Chemistry Reviews* 2021;426:213544. <https://doi.org/10.1016/j.ccr.2020.213544>.
- [170] Liu J, Zou R, Zhao Y. Recent developments in porous materials for H_2 and CH_4 storage. *Tetrahedron Letters* 2016;57:4873–81. <https://doi.org/10.1016/j.tetlet.2016.09.085>.
- [171] Petit C. Present and future of MOF research in the field of adsorption and molecular separation. *Current Opinion in Chemical Engineering* 2018;20:132–42. <https://doi.org/10.1016/j.coche.2018.04.004>.
- [172] Suh MP, Park HJ, Prasad TK, Lim D-W. Hydrogen Storage in Metal–Organic Frameworks. *Chem Rev* 2012;112:782–835. <https://doi.org/10.1021/cr200274s>.
- [173] Lee Y-G, Moon HR, Cheon YE, Suh MP. A Comparison of the H_2 Sorption Capacities of Isostructural Metal-Organic Frameworks With and Without Accessible Metal Sites: $[\{\text{Zn}_2(\text{abtc})(\text{dmf})_2\}_3]$ and $[\{\text{Cu}_2(\text{abtc})(\text{dmf})_2\}_3]$ versus $[\{\text{Cu}_2(\text{abtc})\}_3]$. *Angew Chem Int Ed* 2008;47:7741–5. <https://doi.org/10.1002/anie.200801488>.

- [174] Liu Y, Guo F, Hu J, Zhao S, Liu H, Hu Y. Entropy prediction for H₂ adsorption in metal–organic frameworks. *Phys Chem Chem Phys* 2016;18:23998–4005. <https://doi.org/10.1039/C6CP04645B>.
- [175] Han SS, Mendoza-Cortés JL, Goddard III WA. Recent advances on simulation and theory of hydrogen storage in metal–organic frameworks and covalent organic frameworks. *Chem Soc Rev* 2009;38:1460. <https://doi.org/10.1039/b802430h>.
- [176] Walton KS, Snurr RQ. Applicability of the BET Method for Determining Surface Areas of Microporous Metal–Organic Frameworks. *J Am Chem Soc* 2007;129:8552–6. <https://doi.org/10.1021/ja071174k>.
- [177] Li H, Eddaoudi M, O’Keeffe M, Yaghi OM. Design and synthesis of an exceptionally stable and highly porous metal-organic framework 1999;402:4.
- [178] Rosi NL, Eckert J, Eddaoudi M, Vodak DT, Kim J, O’Keeffe M, et al. Hydrogen Storage in Microporous Metal-Organic Frameworks. *Science* 2003;300:1127–9. <https://doi.org/10.1126/science.1083440>.
- [179] Viswanathan B. Hydrogen Storage. *Energy Sources*, Elsevier; 2017, p. 185–212. <https://doi.org/10.1016/B978-0-444-56353-8.00010-1>.
- [180] Balderas-Xicohténcatl R, Schlichtenmayer M, Hirscher M. Volumetric Hydrogen Storage Capacity in Metal–Organic Frameworks. *Energy Technology* 2018;6:578–82. <https://doi.org/10.1002/ente.201700636>.
- [181] Balderas-Xicohténcatl R, Schmieder P, Denysenko D, Volkmer D, Hirscher M. High Volumetric Hydrogen Storage Capacity using Interpenetrated Metal–Organic Frameworks. *Energy Technology* 2018;6:510–2. <https://doi.org/10.1002/ente.201700608>.
- [182] Jouyandeh M, Tikhani F, Shabaniyan M, Movahedi F, Moghari S, Akbari V, et al. Synthesis, characterization, and high potential of 3D metal–organic framework (MOF) nanoparticles for curing with epoxy. *Journal of Alloys and Compounds* 2020;829:154547. <https://doi.org/10.1016/j.jallcom.2020.154547>.
- [183] Lyle S, Flaig R, Cordova K, Yaghi O. Facilitating Laboratory Research Experience Using Reticular Chemistry. *Journal of Chemical Education* 2018;95. <https://doi.org/10.1021/acs.jchemed.8b00265>.
- [184] Gomez LF, Zacharia R, Bénard P, Chahine R. Simulation of Binary CO₂/CH₄ Mixture Breakthrough Profiles in MIL-53 (Al). *Journal of Nanomaterials* 2015;2015:1–15. <https://doi.org/10.1155/2015/439382>.
- [185] Gómez-Gualdrón DA, Wang TC, García-Holley P, Sawelewa RM, Argueta E, Snurr RQ, et al. Understanding Volumetric and Gravimetric Hydrogen Adsorption Trade-off in Metal–Organic Frameworks. *ACS Appl Mater Interfaces* 2017;9:33419–28. <https://doi.org/10.1021/acsami.7b01190>.
- [186] Schlichtenmayer M, Hirscher M. Nanosponges for hydrogen storage. *J Mater Chem* 2012;22:10134. <https://doi.org/10.1039/c2jm15890f>.
- [187] Schlichtenmayer M, Hirscher M. The usable capacity of porous materials for hydrogen storage. *Appl Phys A* 2016;122:379. <https://doi.org/10.1007/s00339-016-9864-6>.

- [188] Yuan D, Zhao D, Sun D, Zhou H-C. An Isoreticular Series of Metal–Organic Frameworks with Dendritic Hexacarboxylate Ligands and Exceptionally High Gas-Uptake Capacity. *Angewandte Chemie International Edition* 2010;49:5357–61. <https://doi.org/10.1002/anie.201001009>.
- [189] Ahmed A, Seth S, Purewal J, Wong-Foy AG, Veenstra M, Matzger AJ, et al. Exceptional hydrogen storage achieved by screening nearly half a million metal-organic frameworks. *Nat Commun* 2019;10:1568. <https://doi.org/10.1038/s41467-019-09365-w>.
- [190] Bastos-Neto M, Patzschke C, Lange M, Möllmer J, Möller A, Fichtner S, et al. Assessment of hydrogen storage by physisorption in porous materials. *Energy Environ Sci* 2012;5:8294–303. <https://doi.org/10.1039/C2EE22037G>.
- [191] Ahmed A, Liu Y, Purewal J, Tran LD, Wong-Foy AG, Veenstra M, et al. Balancing gravimetric and volumetric hydrogen density in MOFs. *Energy Environ Sci* 2017;10:2459–71. <https://doi.org/10.1039/C7EE02477K>.
- [192] Minuto FD, Balderas-Xicohténcatl R, Policicchio A, Hirscher M, Agostino RG. Assessment methodology of promising porous materials for near ambient temperature hydrogen storage applications. *International Journal of Hydrogen Energy* 2018;43:14550–6. <https://doi.org/10.1016/j.ijhydene.2018.06.004>.
- [193] Allendorf MD, Hulvey Z, Gennett T, Ahmed A, Autrey T, Camp J, et al. An assessment of strategies for the development of solid-state adsorbents for vehicular hydrogen storage. *Energy Environ Sci* 2018;11:2784–812. <https://doi.org/10.1039/C8EE01085D>.
- [194] Ahluwalia RK, Peng JK. Automotive hydrogen storage system using cryo-adsorption on activated carbon. *International Journal of Hydrogen Energy* 2009;34:5476–87. <https://doi.org/10.1016/j.ijhydene.2009.05.023>.
- [195] Siegel D, Hardy B. Engineering an Adsorbent-Based Hydrogen Storage System: What Have We Learned?, HSECoE Team.; 2021.
- [196] Hurst KE, Gennett T, Adams J, Allendorf MD, Balderas-Xicohténcatl R, Bielewski M, et al. An International Laboratory Comparison Study of Volumetric and Gravimetric Hydrogen Adsorption Measurements. *ChemPhysChem* 2019;20:1997–2009. <https://doi.org/10.1002/cphc.201900166>.